Natural Hazards
https://doi.org/10.1007/s11069-025-07701-6

ORIGINAL PAPER

# Optimisation and application of a high-resolution shallow landslide model at regional scale

**Christoph Schaller[1,2] · Luuk Dorren[1] · Denis Cohen[3,4] · Arie C. Seijmonsbergen[2] · E. Emiel van Loon[2]**

Received: 16 May 2025 / Accepted: 13 September 2025


**Abstract**
Shallow landslides pose a risk to infrastructure and inhabited areas. Regional landslide hazard mapping and modelling are important tools for indicating potential hazard areas. We developed a methodology to assess the absolute shallow landslide occurrence probabilities at regional scale in the canton of Bern, Switzerland. Relative failure probabilities from slope stability simulations, using the probabilistic model SlideforMAP and rainfall scenarios with different return periods, are combined. These values are then normalised by the number of historical landslides observed in an area to obtain an absolute landslide occurrence probability. We parametrised the simulations using soil property classes derived from machine learning (ML)-based soil property maps, ML-based landslide thickness, forest structure data based on individual tree detection, and modelled extreme point precipitation scenarios. A global sensitivity analysis, using Sobol indices for 608 hectare plots with observed landslides distributed throughout the canton, revealed that soil cohesion, angle of internal friction, and forest effect were the most influential parameters. We then optimised the three most important soil parameters, using the Levenberg-Marquardt algorithm, to maximise the Area Under the Curve ($AUC$) for 1216 hectare plots with and without observed landslides. We tested our methodology in four catchments of about 40 $\mathrm{km}^2$ in different regions of Bern, resulting in $AUC$ values ranging from 0.59 to 0.82. The best parametrisations based on optimisation performed similarly to those based on expert input. With plausible spatial distributions and return periods, our methodology can produce information suitable for practical applications, such as hazard indication mapping.

**Keywords** Shallow landslides · Regional hazard mapping · Landslide susceptibility · Soil properties optimisation

## 1 Introduction

In recent years, there has been a significant increase in damage to infrastructure and inhabited areas worldwide due to hydrologically related natural hazards, including hydrologically triggered shallow landslides (Froude and Petley 2018; Swiss Re Institute 2019; Emberson

Extended author information available on the last page of the article

et al. 2020). This has been attributed to an increase in urbanisation in hazard-prone areas and heavy precipitation events. In Switzerland, landslides regularly cause extensive infrastructure damage and closures, evacuations, and even casualties. Between 1946 and 2023, 78 people died as a result of 43 landslide and debris flow events (Badoux et al. 2016; WSL 2019). However, improvements in hazard assessment and mitigation measures have led to a considerable reduction in the number of casualties caused by shallow landslides in recent decades (Badoux et al. 2016; BAFU 2024). Regional landslide hazard mapping and modelling provide an important basis for indicating potential hazard areas and mitigating the risk of these hazards (Dahl et al. 2010; Kaur et al. 2019; Shano et al. 2020; Di Napoli et al. 2021).

Rainfall-induced shallow landslides are one of the most important and dangerous types of mass movement in mountainous regions (Varnes 1978). Shallow landslides often result in hillslope debris flows, which can be very destructive due to their velocity and resulting impact pressure (Zimmermann et al. 2020). Shallow landslides are defined as the movement of a mass of rock or soil along a slope with a sliding surface at a depth of up to 2 m (Varnes 1978; Hungr et al. 2014; Lateltin et al. 2005). In particular, the term "shallow landslide" typically refers to translational sliding movements of soil material (earth and/or debris) from the upper soil layers, characterised by a well-defined sliding surface (Cruden and Varnes 1996; Hungr et al. 2014).

The predisposing factors for the occurrence of shallow landslides include slope gradient, slope morphology, and soil geotechnical properties, which are generally related to the underlying geology (Hungr et al. 2014; Watakabe and Matsushi 2019; Chinkulkijniwat et al. 2019). Most landslides occur in wet, (partially) saturated soils and are triggered by water input due to rainfall or seismic activity (Leonarduzzi et al. 2017; Schuster and Wieczorek 2018). An increase in soil water content causes a reduction in soil shear strength, leading to the failure of the soil material within a shear band. This is usually located at the interface of below-ground discontinuities, such as between regolith (i.e. the unconsolidated material above the bedrock) and bedrock (Catani et al. 2010; Zhang et al. 2017; Xiao et al. 2023), or between layers with different soil characteristics (Li et al. 2013; Ali et al. 2014; Ran et al. 2018; Chinkulkijniwat et al. 2019). The occurrence of shallow landslides is influenced by the soil's hydrological properties and the local hydrological conditions, including the rainfall characteristics, upslope runoff patterns, groundwater levels, and pore-water pressure, (Caine 1980; Iverson 2000; Guzzetti et al. 2008; Li et al. 2013; Chinkulkijniwat et al. 2019). Vegetation can influence landslide occurrence through both hydrological and mechanical processes (Murgia et al. 2022; DiBiagio et al. 2024). It affects the effective soil moisture through interception, increased evapotranspiration, and increased infiltration (Greenway 1987; Chirico et al. 2013; Masi et al. 2021; Murgia et al. 2022; Greco et al. 2023; DiBiagio et al. 2024). Among the mechanical effects, root reinforcement-through the tensile strength of the root network and its interaction with the soil and/or bedrock-is an important factor in the failure criterion on vegetated slopes (Greenway 1987; Schwarz et al. 2010; Dazio et al. 2018; DiBiagio et al. 2024).

Various methods are used to model landslide susceptibility, based on inputs such as disposition factors and landslide inventories, as well as knowledge of hydrological and physical processes (Reichenbach et al. 2018; Murgia et al. 2022). Research has focused on quantitative approaches that produce numerical estimates and probabilities of landslide occurrence in a given area (Guzzetti et al. 1999; Reichenbach et al. 2018; DiBiagio et al. 2024). These quantitative approaches can be divided into three categories: conceptual models, physically

based models, and empirical models (data-driven models) (Murgia et al. 2022). Conceptual models aim to provide a simplified methodology for estimating changes in slope stability (Murgia et al. 2022), e.g. by using cellular automaton models (Piegari et al. 2006). Physically based models can be further divided into deterministic (e.g. Montgomery and Dietrich 1994; Baum et al. 2002) and probabilistic models (e.g. Pack et al. 1998; Horton et al. 2013; van Zadelhoff et al. 2022). Empirical models predict landslide occurrence based on factors that may be directly or indirectly linked to slope instability (Reichenbach et al. 2018). They include statistically based models and AI/machine learning (ML) models (Reichenbach et al. 2018; Murgia et al. 2022). Such models are becoming more commonplace due to improved data availability and quality, increased research in ML and other computational techniques, and improvements in computing and storage technology (Hengl et al. 2017; Merghadi et al. 2020; Wadoux et al. 2020; Ado et al. 2022; Singh et al. 2023; Xiao et al. 2023).

SlideforMAP (SFM), that we first presented in van Zadelhoff et al. (2022), is a physically based probabilistic model that allows for a regional assessment of shallow landslide probability, taking into account the effect of forest cover by considering root reinforcement based on the root bundle model (Cohen et al. 2009; Cohen and Schwarz 2017; Gehring et al. 2019; van Zadelhoff et al. 2022). SFM uses a probabilistic approach by generating hypothetical landslides with a uniform random distribution. Using the limit equilibrium approach, a factor of safety (i.e. the ratio of destabilising forces to stabilising forces) is calculated for the generated landslides. If the factor of safety falls below 1, the hypothetical landslide is considered unstable (i.e. a slope failure would occur). SFM then calculates an index for landslide probability based on the ratio of unstable landslides to the total number of generated landslides. This study aims to improve the application of SFM for regional-scale assessment of shallow landslide occurrence probability. The innovation of this study lies in the combination of automated parameter optimisation, physically based regional slope stability modelling, and the methodology for calculating absolute landslide occurrence probabilities. We pose three research questions: firstly, what are the most sensitive parameters of the SFM model, and how do they relate to the impact of forests? Secondly, how do parametrisations of the most sensitive SFM parameters based on expert input perform compared to an automatic optimisation procedure? Thirdly, how does our SFM-based methodology perform in regional applications with different geological and topographical settings? To answer these questions, we combine data from various relevant sources to parametrise SFM, followed by a sensitivity analysis, an automatic parameter optimisation procedure, a comparison with expert-based parameter estimates, and an evaluation in four distinct regions.

## 2 Study area

The study area is the canton of Bern (total area 5959 $\mathrm{km}^2$) in Switzerland (Fig. 1). Approximately 32% of its area is covered by forests, 30% by other (semi-)natural areas (shrubs, grasslands, moors, and wetlands), 28% by agricultural areas, 7% by artificial surfaces, and 3% by water bodies (FSO 2024). The landscape can be roughly divided into four regions: the Jura, the Central Plateau, the pre-Alps, and the Alps. The Jura Mountains in the north are mainly characterised by limestone and marl formations (Pfiffner 2021; Zappone and Kissling 2021). The Central Plateau, which extends from the Jura piedmont in the north to the pre-Alps in the south, is a molasse basin filled with thick Quaternary deposits resulting

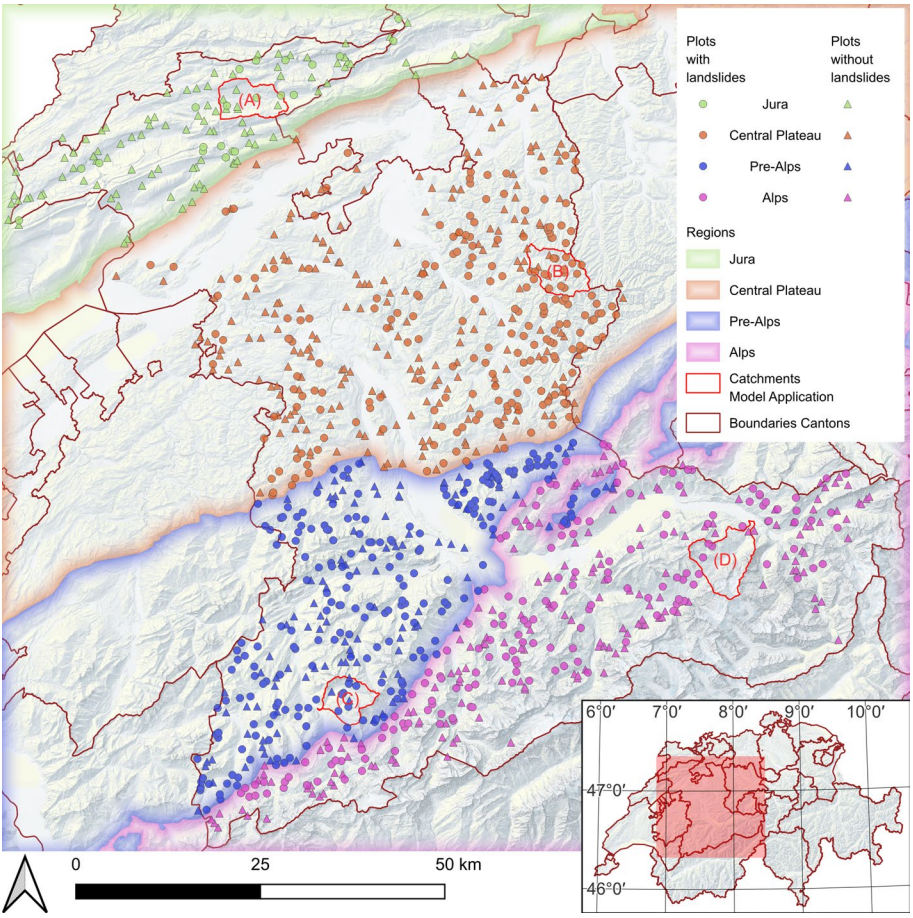


**Fig. 1** Map showing the locations of the plots with (circles) and without (triangles) observed landslides in the canton of Bern, which were used for the sensitivity analysis and optimisation. The catchments for the application of the methodology are shown in red (see Fig. 2 for details). The Jura, Central Plateau, the pre-Alps, and Alps are indicated in the same colours as the corresponding plots. Background: swissBOUNDARIES3D (Swisstopo 2024c), and light base map relief (Swisstopo 2024a)

from the erosion of the Alpine chain (Reynard et al. 2021). The Bernese Alps consist mainly of the Helvetic and Penninic nappes; parts of these nappes are referred to as the pre-Alps (see Fig. 1), which include lower mountain ranges and also foothills in the northernmost parts. The Alpine nappes consist of continental and oceanic basement rocks (granite, gneiss, and schist formations); shallow-marine carbonates (limestone and marl formations); deep-marine clastics (sandstone and conglomerate formations), including local turbidite deposits known as flysch; and radiolarian chert (Pfiffner 2021). The canton of Bern has a temperate semi-continental climate that is strongly influenced by its altitude and complex topography (Fallot 2021). The mean annual air temperature varies with altitude, ranging from 8.5−11.9 °C at 500 m above sea level, 6.2−9.6 °C at 1000 m, and 3.9−7.3 °C at 1500 m over the period from 1981–2010 (Fallot 2021). The mean annual rainfall increases with altitude, with values of 900–1300 mm for the Central Plateau, and gradually increases from the southern

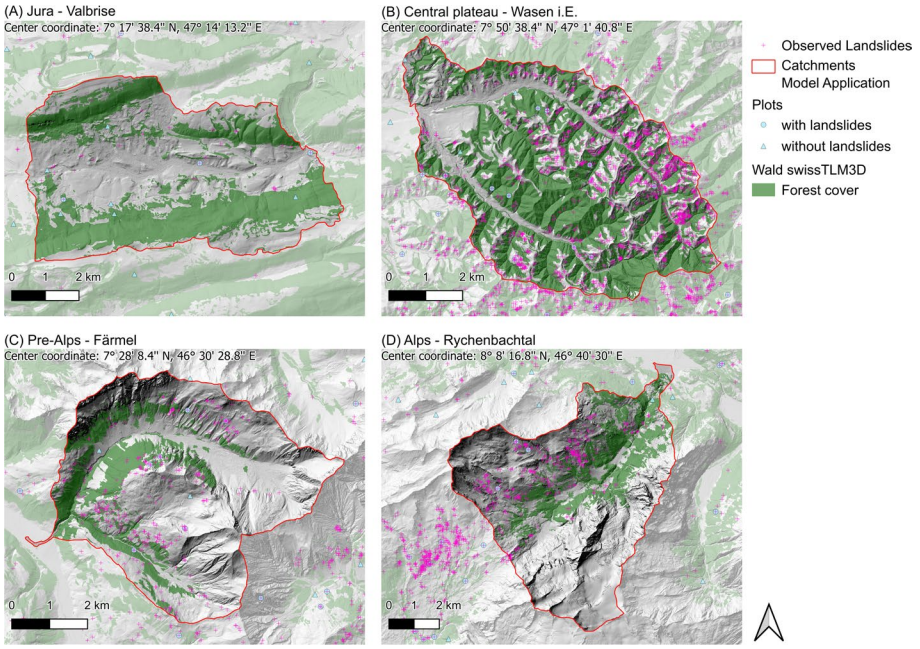


**Fig. 2** Maps showing the catchments used to test the methodology for assessing absolute landslide occurrence probabilities. Observed historical landslides are shown as purple crosses. Background: swissBOUNDARIES3D (Swisstopo 2024c), swissTLM3D ground cover forest (Swisstopo 2023b), and swissALTI3D monodirectional hillshade (Swisstopo 2024b)

**Table 1** Characteristics of the catchments used to test the methodology for assessing absolute landslide occurrence probabilities at regional scale

| Region | Name | Number of observed landslides | Slide density [slides per $km^2$] | Surface area [$km^2$] | Elevation (m a.s.l.) | Mean slope [°] | Forest cover [%] |
|---|---|---|---|---|---|---|---|
| (A) Jura | Valbrise | 31 | 0.81 | 38.5 | 665–1336 | 14.95 | 42 |
| (B) Central plateau | Wasen i.E | 1503 | 39.23 | 38.3 | 739–1383 | 27.26 | 55 |
| (C) Pre-Alps | Färmel | 311 | 10.04 | 31.0 | 1006–2762 | 29.47 | 17 |
| (D) Alps | Rychenbachtal | 335 | 6.37 | 52.6 | 668–3702 | 29.69 | 18 |

piedmont of the Jura Mountains towards the northern side of the Alps, where it exceeds 2000 mm, reaching up to 3000 mm or more per year on some summits in the Central Alps.

Square plots measuring 1 ha were selected for the sensitivity analysis and optimisation. This selection was based on homogeneous terrain units in the form of microcatchments (averaging 26.2 ha (Hählen 2024)). Based on stratified random sampling of the microcatchments (stratification by the four regions), we selected 608 plots with observed landslides and 608 plots without landslides, which were spatially well distributed throughout the canton (see Fig. 1). In each of the four regions, a catchment of approximately 40 $km^2$ was selected to test the application of our methodology (see Fig. 2). The different topographies, geologies, and land covers of these catchments are representative of each region (Table 1). The Valbrise catchment is located in the folded Jura, with geology consisting of sedimen-

tary rocks and molasse deposits at the valley bottom. The Wasen catchment, located in the Emmental, lies within the Central Plateau and has a hilly terrain formed by molasse deposits. The Färmel catchment in the pre-Alps lies within the Penninic nappe, with its geology dominated by sedimentary rocks and Mesozoic mélange. The Rychenbachtal in the Alps lies within the Helvetic nappe system. Its northern part, where historical landslides have been observed, is dominated by sedimentary rocks including melange and flysch. The southern part forms part of the Aare massif, which is dominated by crystalline rocks.

## 3 Materials

### 3.1 Landslide inventory

As reference data, we used an inventory of observed shallow landslides created by the canton of Bern's Office for Forests and Natural Hazards (Hählen 2024). This inventory contains entries with points in the Swiss LV95 coordinate system based on recorded events and events identified from orthoimagery between 1962 and 2024. Of the 25,039 landslides included in the data, 20,724 were manually digitised from orthoimagery. In addition, the dataset included the microcatchments delimiting coherent terrain units used for plot selection (Hählen 2024). A second inventory by Hählen (2023) was used to parametrise the inverse gamma distribution, proposed by Malamud et al. (2004), to generate landslide areas in SFM (van Zadelhoff et al. 2022). This inventory includes 519 landslides in the canton of Bern, recorded between 2005 and 2021. It includes the failure zones and runout envelopes of manually digitised polygons from orthoimagery.

### 3.2 Model input data

The simulations in this study were driven by the following datasets. Section 4 explains the detailed use of the datasets:

- Light detection and ranging (LiDAR)-based swissALTI3D digital elevation model (DEM) with a cell size of 0.5 m (Swisstopo 2023a);
- Individual trees detected from a LiDAR-based canopy height model (CHM) with a cell size of 1 m (Schaller et al. 2023);
- National Forest Inventory (NFI) forest type raster 2018 with a cell size of 10 m, indicating the proportion of coniferous trees (cf. Schaller et al. 2023);
- Modelled extreme point precipitation data (Frei and Fukutome 2022) with a cell size of 1 km for different return periods (2, 10, 30, 50, 100, 200, and 300 years);
- Soil property maps with a cell size of 30 m (a preliminary version, kindly provided by the Swiss Competence Center for Soils (CCSol 2024)), providing predictions for clay, sand, and silt contents at 0–30 cm, 30–60 cm, and 60–120 cm (Stumpf et al. 2024);
- Tectonic map of Switzerland (Swisstopo 2024d);
- The ground cover layer from swissTLM3D (Swisstopo 2023b);
- Topographic catchment areas of Swiss water bodies (BAFU 2019).

## 4 Methods

Our workflow was divided into the following five stages (Fig. 3):

1. Input data for the simulations were prepared. This included the DEM, flow accumulation, landslide thickness, and soil class rasters, as well as forest structure data.
2. Plots and catchments used in the subsequent stages were selected, and their individual simulation inputs were prepared.
3. A global sensitivity analysis of selected SFM parameters was performed based on simulations on plots with observed landslides.
4. The most sensitive parameters, excluding the forest, which was taken as is, were optimised based on plots with and without observed landslides.
5. The methodology for assessing absolute landslide probabilities was applied to simulations in the four 40 $\mathrm{km}^2$ catchments using parametrisations based on the results from stage 4, as well as expert-based input.

All stages were implemented in Python (van Rossum and Drake 2009), except for the prediction of landslide thickness, which was implemented in R (R Core Team 2022). The code for the entire process can be found in the accompanying repository for this study (Schaller 2025). Geodata processing was implemented using the Geospatial Data Abstraction Library (GDAL) tools (GDAL/OGR contributors 2021) via the GDAL Python bindings. Some steps

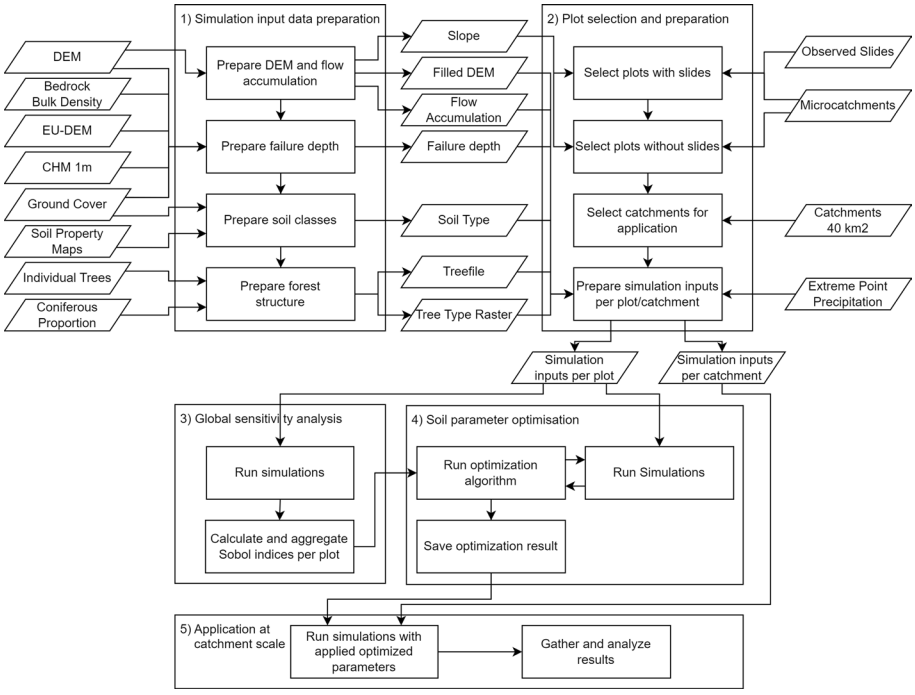


**Fig. 3** Flowchart of the methodology. The five separate boxes describe the 1) simulation input data preparation, 2) plot selection and preparation, 3) global sensitivity analysis, 4) soil parameter optimisation, and 5) application at catchment scale

were implemented using the System for Automated Geoscientific Analyses (SAGA) GIS (Conrad et al. 2015) through its command-line interface. The slope stability simulations were performed by calling the command-line version of SFM (van Zadelhoff et al. 2022) from Python.

### 4.1 Simulation input data preparation

In the first stage, all inputs required for SFM simulations were generated for the entire canton of Bern, to be used as input for the second stage.

#### 4.1.1 DEM and flow accumulation

Slope stability simulations were performed using a DEM with a cell size of 2 m, as this resolution has shown to be a good compromise between the level of detail and processing time. The original 0.5 m cell size swissALTI3D DEM (Swisstopo 2023a) was first aggregated to a 2 m cell size using gdalwarp with the AVERAGE function. This aggregated DEM was then sink-filled using the SAGA GIS tool "Module Fill Sinks XXL (Wang & Liu)" based on the method of Wang and Liu (2006). This hydrologically corrected DEM was the basis for the DEM rasters used in the simulations. It was also used to derive the flow accumulation - the second DEM-based SFM input - by applying the SAGA GIS tool "Module Flow Accumulation (Top-Down)" with the deterministic 8 algorithm (O'Callaghan and Mark 1984).

#### 4.1.2 Landslide thickness

The SFM parameter for the landslide failure depth was parametrised by specifying a raster with landslide thickness values. The standard deviation for the thickness was set to 0. The thickness values were generated by applying the random forest-based model, which was trained using data from Rickli et al. (2016, 2019), as described by Schaller et al. (2025). Based on the resolution used by the ML model, the necessary input data were prepared as 5 m cell size rasters using R (R Core Team 2022) and SAGA GIS, before the trained model was applied to predict the landslide thickness. The processing was performed using tiles based on catchment areas aggregated to approximately 150 $\mathrm{km}^2$ (BAFU 2019). The individual prediction tiles were merged into a single thickness raster covering the canton of Bern. The prediction raster was resampled to a 2 m cell size using the nearest neighbour function in gdalwarp (GDAL/OGR contributors 2021), generating the input raster for the simulations.

#### 4.1.3 Soil classes

The soil classes used to define the physical properties of the soil in the SFM simulations were specified using rasters with a cell size of 2 m. For the sensitivity analysis, a raster with a single, uniform soil class was generated for the entire study area. For the optimisation and application of the soil parameters, a differentiated soil class raster was derived from soil property maps with a cell size of 30 m, which provided predictions for clay, sand, and silt contents at 0–30 cm, 30–60 cm, and 60–120 cm depth (Stumpf et al. 2023). First, the clay, sand, and silt content at the predicted landslide thickness was determined from the soil

property maps. One of the 12 major United States Department of Agriculture (USDA) soil texture classes (see supplementary material A.2) was assigned to each cell by comparing the determined values for clay, sand, and silt content to the corresponding values defined by the Natural Resources Conservation Service (NRCS) soil texture calculator (Newville et al. 2024). As the soil property maps do not contain data for areas without soil cover (e.g. settlements, rock, glaciers, and water), a separate *NoSlide* class was applied to these areas. The resulting raster was then smoothed with a 15 m radius majority filter using SAGA GIS. In the smoothed raster, all areas with a slope gradient >50°, or classified as "rock" ("Fels") or unconsolidated rock ("Lockergestein") in the swissTLM3D ground cover (Swisstopo 2023b), were reclassified as *NoSlide*. Finally, the soil class raster was combined with a forest mask based on "forest" ("Wald") and "open forest" ("Wald offen") classes from the swissTLM3d ground cover, in order to distinguish soil classes within and outside of the forest, resulting in a raster containing 26 potential soil classes.

A table was compiled that includes the parameter values for the physical properties per soil class (see Table A3). It includes default values, as well as the minimum and maximum values for the parameters to be optimised. The default values are based on expert input and take into account references from standards and literature, as well as experience from applying SFM in practice. As most reference materials for the soil physical properties use the Unified Soil Classification System (USCS), the USDA soil texture classes were assigned a USCS class based on the consensus in Table 17 of García-Gaines and Frankenstein (2015) (see supplementary material A.3). The values of soil cohesion and angle of internal friction per soil class were based on those given in the works of Dysli and Rybisar (1992) and VSS SN (1998). The range of conductivity values is based on the values from Dysli and Rybisar (1992) and Rüegger and Hufenus (2003). The soil class values inside and outside the forest are identical, except that the hydraulic conductivity is increased by 700 m/d, based on expert interpretation of ring infiltration tests in the field. This reflects the fact that tree roots significantly increase conductivity, thereby contributing to a reduction in failure probability (Alaoui et al. 2011; Chandler et al. 2018; May et al. 2024). The *NoSlide* soil class parameters enforce stable slopes in the SFM simulations.

#### 4.1.4 Forest structure

We used coordinates and diameter at breast height (DBH) of single trees to account for the stabilising effect of the forest (cf. Murgia et al. 2022; van Zadelhoff et al. 2022). These were derived from the detection of individual trees in a canopy height model (CHM) using local-maxima detection (Schaller et al. 2023). As data on individual tree species were not available, we assigned one tree species per plot based on the 2018 NFI forest type raster (Waser and Ginzler 2018). This raster, which has a cell size of 10 m, indicates the proportion of coniferous trees. We derived a tree type raster by resampling the NFI forest type to a cell size of 2 m, classifying cells with a value of less than 50% as broadleaved-dominated and those with a value of more than 50% as coniferous.

### 4.2 Plot selection and preparation

In the second stage, plots used in stages 3 and 4 and catchment areas used in stage 5 were selected. Individual simulation inputs were then derived for the plots and catchments.

### 4.2.1 Selecting plots for sensitivity analysis and optimisation

A set of hectare plots with observed landslides and a set without observed landslides were selected for stages 3 and 4 (Table 2). The selection criteria and steps differed slightly between the two sets:

1. Selection of microcatchments based on criteria:
   - Contains slopes of at least 15°
   - Stratified by region
   - Plots with landslides:
     - Select 10% of microcatchments containing observed landslides
   - Plots without landslides:
     - Select a matching number of microcatchments containing no observed landslides
2. Generation of candidate plots:
   - Plots with landslides:
     - Generate hectare-sized plots around the centroids of clusters derived by clustering landslide points using DBSCAN (Ester et al. 1996) with a radius 50 m
   - Plots without landslides:
     - Generate a regular hectare grid over the microcatchment
3. Selection of plots from candidates based on criteria:
   - Contain slopes of at least 15°
   - 1 plot per selected microcatchment
   - Plots with landslides:
     - Select the plot of the largest cluster in the microcatchment

**Table 2** Plots used for sensitivity analysis and optimisation by region

| Region | Plots with observed landslides | | Plots without landslides | |
|---|---|---|---|---|
| | Total | Forest ≥ 50% | Total | Forest ≥ 50% |
| Jura | 21 | 5 | 99 | 62 |
| Central plateau | 208 | 72 | 223 | 95 |
| Pre-Alps | 218 | 79 | 114 | 52 |
| Alps | 161 | 58 | 172 | 83 |
| Total | 608 | 214 | 608 | 292 |

- Plots without landslides:
  - Exclude plots where the majority of the soil class is *NoSlide*
  - Select a random plot in the microcatchment

For both sets, we first randomly selected microcatchments, stratified by region. Then we generated candidate plots within these microcatchments and finally selected the actual plots from these candidates. The four regions (Jura, Central Plateau, pre-Alps, and Alps, as shown in Fig. 1) were assigned based on local knowledge and geometries digitised based on geological units in the 1:500000 scale tectonic map (Swisstopo 2024d). As landslides typically occur on slope gradients of more than 15° (Schaller et al. 2025), only microcatchments and plots containing slopes of at least 15° (at 10 m cell size) were considered. Finally, we selected 10% of the microcatchments meeting the criteria for plots with landslides (n = 6123) and an equal number of plots for microcatchments without landslides (n = 17,980).

#### 4.2.2 Selecting catchments for application

The catchments in which we applied our methodology in stage 5 were selected from predefined catchments aggregated to approximately 40 $\mathrm{km}^2$ (BAFU 2019). One catchment was selected within each region. We selected catchments that were completely contained within the region, and whose topography and geology we considered representative of that region. Catchments with high observed landslide activity were given preference.

#### 4.2.3 Preparing simulation inputs

After selecting the plots and catchments, the corresponding simulation inputs were derived from the prepared input data. As boundary effects can lead to increased failure probabilities at the edge of the simulation raster, plot perimeters were buffered by 50 m during input preparation. These buffered perimeters were then used to create clipped rasters for each plot using the canton-wide DEM, contributing area, soil class, and landslide thickness rasters (see supplementary material A.1 for maps of simulation inputs). Individual tree files for each plot were created by extracting points from the tree detection within the buffered perimeter. Additionally, a configuration file with default values for the simulations was generated for each plot. Subsequent simulations modified these default values in the configuration files, e.g. by adjusting the rainfall amount or the soil physical properties according to the scenario.

If the tree file contained trees, the corresponding path and the option to simulate with forest effect were set in the configuration. Tree species were selected by determining the majority value within the tree type raster. Plots with a majority of broadleaved-dominated cells were assigned *Fagus sylvatica* (European beech) as the species or otherwise *Picea abies* (Norway spruce).

For the rainfall scenarios, values were determined for extreme point precipitation events with return periods *RP* of 2, 10, 30, 100, or 300 years (Frei and Fukutome 2022). For the hectare plots, the rainfall rate value $R_{RP\_97.5}$ was obtained by sampling values at the plot centre from the 97.5th percentile prediction rasters of the 24-hour rainfall amount. For the catchments used in stage 5, the rainfall amount was calculated as the mean value within each

catchment using a zonal statistic. The rainfall rate $R_{RP}$ in [mm/h], as specified in the model configuration, was then calculated as

$$R_{RP} = \frac{R_{RP\_97.5} * rc_{RP}}{24} \quad (1)$$

where the runoff coefficient $rc_{RP}$ (2 yr: 10%, 10 yr: 12%, 30 yr: 14%, 100 yr: 20%, 300 yr: 30%) takes into account the fact that in saturated soils, only a portion of rainfall that is neither absorbed by infiltration into deeper soil layers nor diverted as surface runoff contributes to the water pressure affecting slope stability. Runoff coefficients were estimated from rainfall experiments conducted across Switzerland and Liechtenstein (May et al. 2024) as well as from practical experience with the application of SFM, where the model was calibrated based on historical rainfall events.

### 4.3 Global sensitivity analysis

In the third stage, we performed a global sensitivity analysis of SFM based on Sobol's method (Sobol' 2001), which is a form of variance-based sensitivity analysis. We used the Python library SALib (Herman and Usher 2017) to compute the Sobol indices. Analysis was performed for two separate simulation runs. The first run included simulations in all 608 plots with observed landslides, varying five soil property and rainfall parameters. To explore the influence of the forest on the model results, the second run was performed with simulations in a subset of 214 plots with at least 50% forest cover. A parameter was added to indicate whether the simulation should be performed with or without forest effect.

Parameters for the sensitivity analysis (see Table 3) were selected based on the results of a previous study (van Zadelhoff et al. 2022) and expert input on the parametrisation of SFM in practical applications. For the parameters relating to soil physical properties, we chose to sample and analyse the mean values for cohesion, field capacity, hydraulic conductivity, porosity, and angle of internal friction. SFM supports additional parameters for standard deviations for cohesion, field capacity, and hydraulic conductivity. We chose to set these parameters to 0. In the second analysis run with the forested plots, sampled values for the forest parameter were rounded to obtain Boolean 0/1 values to indicate simulation with or without forest effect.

Model inputs for the parameters were generated using Saltelli's extension (Saltelli 2002) of Sobol's sequence (Sobol' 2001) implemented in SALib. A sample size of n=1024 was used, resulting in 14,336 combinations for the first run with six parameters, and 16,384

**Table 3** Parameters and ranges of values used in the sensitivity analysis, indicated by minimum and maximum values

| Parameter | Description | Minimum | Maximum |
|---|---|---|---|
| c | Mean soil cohesion [kPa] | 0 | 5 |
| fc | Mean soil field capacity | 0.1 | 0.4 |
| ks | Mean soil hydraulic conductivity [m/d] | 0.000864 | 8640 |
| por | Mean soil porosity | 0.25 | 0.75 |
| r | Mean angle of internal friction [°] | 20 | 45 |
| Rainfall | Rainfall amount in [mm/h] | 0.1 | 5 |
| Forest | Simulation with forest | 0 | 1 |

combinations for the second run with seven parameters, on the forested plots. Separate slope stability simulations were performed for each plot and parameter combination. These simulations assumed a uniform soil class across all plots, with physical properties based on the respective parameter combinations. The number of failed landslides within the plot (or within the forest for the second run) was determined as the outcome of each simulation.

These results were then used to calculate the total-, first-, and second-order Sobol indices for each plot. First-order indices measure the contribution to output variance by a single parameter, while second-order indices measure the interaction between two parameters. Total-order indices account for both first-order effects and all interactions. SALib calculates first- and total-order indices based on Saltelli et al. (2010), while the estimation of the second-order sensitivities follows Saltelli (2002). Finally, the calculated indices were aggregated across all plots to obtain a global sensitivity value. The aggregation follows the formulation for generalised Sobol indices by Gamboa et al. (2013):

$$S_i = \frac{\sum_{j=1}^{p} \mathrm{V}ar(Y_j) \cdot S_i^j}{\sum_{j=1}^{p} \mathrm{V}ar(Y_j)} \tag{2}$$

where $S_i$ is the generalised Sobol index *i* ($i \in \{total, 1, 2\}$), $Y = (Y_1, ...., Y_p)^T$ is the result vector of our simulations, where *p* is the number of simulated plots, $\mathrm{V}ar(Y_j)$ is the variance of the *j*th plot, and $S_i^j$ is the Sobol index *i* of the *j*th plot. Since estimated index values close to zero can become negative for numerical reasons (Saltelli et al. 2010), negative index values with confidence intervals overlapping zero were treated as zero in the aggregation.

### 4.4 Soil parameter optimisation

In the fourth stage, three soil parameters identified as the most important in the sensitivity analysis were optimised. The optimisation procedure used the Levenberg-Marquardt (LM) algorithm provided by the lmfit Python library (Moré 1978; Newville et al. 2024), which allows bounds to be specified on the optimisation parameters.

The mean cohesion (c), mean angle of internal friction (r) and mean hydraulic conductivity (ks) were selected for optimisation due to their high sensitivity values and their role in the SFM model. Despite having similar sensitivity values to hydraulic conductivity, mean porosity was not selected for optimisation, as it is only used to determine soil bulk density in the model and therefore only influences the result indirectly via soil mass. Only the parameters of soil classes 3, 4, 7, and 8 were optimised, as these represent the majority of cells in the canton of Bern and the selected plots. The parameter values of the corresponding soil classes within the forest (classes 23, 24, 27, and 28) were kept the same as the values of the four soil classes outside the forest, except that a constant of 700 m/d was added to the hydraulic conductivity. This resulted in a total of 12 parameters being optimised. The impact of the forest itself was not selected for optimisation as the existing forest is assumed to be a fixed, given parameter in the simulations.

We tested various combinations of initial values and optimisation configurations. Based on the values in Table A3, we set the initial values to the values based on expert input, the minimum value, maximum value, or midpoint of the value range. Initial tests showed that the *epsfcn* parameter of the optimisation method, which is used to determine an appropriate step length for the forward-difference approximation of the Jacobian matrix, needed to be

increased. Otherwise, the variation of the parameters by the optimisation algorithm was too small to influence the result, causing the process to quickly stop without changing the input parameters. Therefore, we tested different values for the *epsfcn* parameter, ranging from 0.01 to 1.

As an objective function, we chose to optimise the Area Under the Curve ($AUC$) of the Receiver Operating Characteristic (ROC) (Metz 1978; Fawcett 2006) by minimising the value of $1 - AUC$ on the individual plots. We used the Scikit-learn Python library (Pedregosa et al. 2011) to calculate the $AUC$ values. For the plots with observed landslides, we first buffered the landslide points within each plot by 5 m and then rasterised them, before calculating the $AUC$ per plot. The resulting binary raster and the failure probability raster generated by the simulations were used as inputs to calculate the $AUC$. For the plots without observed landslides, we generated two points per plot using a uniform random distribution to approximate the mean number of observed landslides per plot. These points were also buffered by 5 m and then rasterised. However, the $AUC$ was then calculated using the resulting binary raster and the raster $1 - failure\_probability$.

The optimiser ran simulations for all plots using a function that runs SFM simulations based on the same methodology as the model application described in Sect. 4.5. The correction factor used in the simulations was calculated by dividing the summed probability in each plot by the mean number of historical landslides per hectare in the surrounding 40 $\mathrm{km}^2$ catchment. To determine the optimisation progress, the optimiser used the $1 - AUC$ values of the plots, which were calculated using the absolute landslide occurrence probabilities resulting from the simulations.

To evaluate the results of the optimisation, we primarily evaluated the sum of the $AUC$ values of all plots. We also calculated the sum for the $1 - AUC$ values. In addition, we included the Akaike Information Criterion (AIC) and the Bayesian Information Criterion (BIC) statistics returned by the optimiser to assess the performance of the resulting model. We used the parameter values and $AUC$ values from the simulation with the initial expert input for comparison.

### 4.5 Application at catchment scale

In the fifth stage, we tested a methodology for deriving absolute landslide probabilities from SFM simulations. For parametrisation, we used selected results from the optimisation and expert input. Based on the overall $AUC$ and the statistics provided by the optimiser, we selected the best result for the optimisations with initial values based on (A) the minimum of the value range, (B) the maximum of the value range, and (C) expert input. We included variant (D) with the initial values based on expert input for comparison.

A single SFM simulation provides relative probabilities of slope failure with respect to a specific rainfall scenario. Therefore, we developed a methodology that combines relative probabilities from rainfall scenarios with different return periods, then normalised them by the number of observed historical landslides in an area, to obtain an absolute landslide occurrence probability for a given observation period. The methodology consists of the following steps:

1. Separate SFM simulations were performed for 2-, 10-, 30-, 100-, and 300-year return period (*RP*) scenarios of 24-hour rainfall corrected with the runoff coefficients

mentioned in Sect. 4.2.3. For the simulations, one landslide per square metre was generated with a size randomly generated from an inverse gamma distribution (Malamud et al. 2004) that was parametrised based on inventory data (Hählen 2023). Each cell may therefore be part of several hypothetical landslides, some of which may become unstable.

2. The relative landslide occurrence probability ($RLOP_{RP_j}$) [0-1] was calculated based on the number of unstable landslides per 2 x 2 m cell (i.e. a factor of safety < 1) divided by the total number of simulated landslides per cell for all *RP*.
3. The sum $RLOP_{sim\_tot}$ of all $RLOP_{RP_j}$ weighted with the occurrence probability of the given return period scenario ($P_{occTperiod,RP}$) during a time period (*TimePeriod*) is

$$RLOP_{sim\_tot} = \sum_{j=1}^{n} (RLOP_{RP_j} \cdot P_{occTperiod,RP_j}) \tag{3}$$

where

$$P_{occTperiod,RP_j} = 1 - \left(1 - \frac{1}{RP_j}\right)^{TimePeriod} \tag{4}$$

For an event with a return period of 2, 10, 30, 100, or 300 years during a period of 62 years (1962-2024), this gives a $P_{occTperiod}$ of 100%, 99.8%, 87.8%, 46.4% and 18.7% respectively.

4. $RLOP_{sim\_tot}$ was aggregated to reference areas using a SUM function, giving $RLOP_{simRA}$. We tested the entire 40 $\mathrm{km}^2$ catchment, the microcatchment, and a regular hectare grid as reference areas. These reference areas were used to calculate the correction factor for the landslide occurrence probabilities.
5. A correction factor $Corr_{NLS}$ for the final failure probabilities computed by SFM was calculated based on the number of observed landslides $NLS_{obs}$ divided by the sum of $RLOP_{simRA}$ in the reference area with the shortest return period (i.e. the highest number of observed landslides) during the observation period:

$$Corr_{NLS} = \frac{NLS_{obs}}{RLOP_{simRA}} \tag{5}$$

6. The release probability $P_{release,RP_j}$ of each cell per *RP* was calculated by multiplying it with the occurrence probability of the $RP_j$ ($P_{occ,RP_j}$):

$$P_{release,RP_j} = RLOP_{RP_j} \cdot P_{occ,RP_j} \tag{6}$$

where $LS_{Prob,RP_j}$ is the spatial landslide probability (or landslide susceptibility) per cell calculated by SFM and $RP_j$ is:

$$P_{occ,RP_2} = \tfrac{1}{2} - \tfrac{1}{10} = 0.4;$$
$$P_{occ,RP_2} = \tfrac{1}{2} - \tfrac{1}{10} = 0.4;$$
$$P_{occ,RP_{10}} = \tfrac{1}{10} - \tfrac{1}{30} = 0.0667;$$

$$P_{occ,RP_{30}} = \frac{1}{30} - \frac{1}{100} = 0.0233;$$
$$P_{occ,RP_{100}} = \frac{1}{100} - \frac{1}{300} = 0.0067;$$
$$P_{occ,RP_{300}} = \frac{1}{300} = 0.0033;$$

Since the minimum selected $RP = 2$ years, the sum of all scenario probabilities = 0.5.

7. The raster with the final result, consisting of the absolute landslide occurrence probability $AbsLS_{Prob}$, based on the cumulated relative probabilities corrected with the real observations, was obtained by:

$$AbsLS_{Prob} = Corr_{NLS} \cdot \sum_{j=1}^{n} P_{release,RP_j} \tag{7}$$

8. For visualisation and analysis purposes, the absolute landslide occurrence probability $AbsLS_{Prob}$ was aggregated to a cell size of 100 m using a SUM function.

For normalisation, we used historical landslides within the simulation perimeter from the inventory created by Hählen (2024), which covers a period of 62 years (1962-2024). We tested the entire 40 $\mathrm{km}^2$ catchment, the microcatchments and a regular hectare grid as reference areas for calculating the correction factor for normalisation. The absolute landslide occurrence probability was calculated at a 2 m cell size by summing the relative probabilities, weighted by the occurrence probability of the scenario return period, and multiplied by the correction factor to normalise the value to the observed landslide frequency. Finally, the absolute landslide occurrence probability was aggregated to a 100 m cell size for visualisation and analysis purposes. This cell size was chosen because it represents the lower limit for a useful area for practical applications and because it results in meaningful return periods.

We calculated the overall $AUC$ and plotted ROC $AUC$ curves for the observed landslides in the catchments buffered by 5 m to evaluate the results of different simulations and correction methods tested during the application. The observed and simulated occurrence probabilities were compared at a regular hectare grid scale.

## 5 Results

### 5.1 Sensitivity analysis

The mean cohesion and the mean angle of internal friction are the most sensitive parameters, with values of 0.34 and 0.24 for the first-order indices in the general sensitivity analysis (Fig. 4). Mean porosity and mean hydraulic conductivity are the third and fourth most sensitive parameters, with significantly lower values of 0.0078 and 0.0052, respectively. The much higher values of 0.71 and 0.62 for the total-order indices for cohesion and angle of internal friction suggest possible interactions. This is supported by the combination of these two parameters showing the highest value by far for the second-order index (see A.5). The results of the sensitivity analysis that include the forest effect are very similar to the results

of the general analysis, with cohesion and angle of internal friction being the most important parameters. However, the forest parameter is the third most important parameter in this analysis, with a first-order index of 0.024, followed by porosity and hydraulic conductivity. The value of 0.12 for the total-order index of the forest parameter also indicates possible interactions. The second-order indices for this analysis suggest weak interactions between forest and cohesion, as well as between forest and angle of internal friction. However, the index values of 0.063 and 0.043 for these combinations are significantly lower than the value of 0.25 for the combination of cohesion and angle of internal friction.

### 5.2 Soil physical property optimisation

Depending on the initial values selected and the *epsfcn* parameter value, the optimisation process terminated after 50–200 function evaluations. Leaving the *epsfcn* parameter at its default value of $1.0 \times 10^{-10}$ resulted in the parameters remaining at their initial values. Testing *epsfcn* values between 0.1 and 1 did affect the optimisation result, but there is no clear optimal value that works best for all initial parameter values.

The reduction in the $Sum(1 - AUC)$ value (or the increase in the *Sum*($AUC$) value) of the optimised results, compared to the expert input, differs between the optimisation runs (Table 4). The optimised results for runs using the expert input as initial values combined with different *epsfcn* values remain close to the values of 557.22 for $Sum(1 - AUC)$ and 658.78 for *Sum*($AUC$) of the initial, non-optimised input. The *Sum*($AUC$) for some runs is even slightly lower. The runs with initial values set to the minimum of the value range show the best overall performance of all optimisations tested (lowest $Sum(1 - AUC)$ and highest *Sum*($AUC$)). This is supported by the lowest overall BIC and AIC values. The runs with initial values in the middle of the value range performed poorly, with all indicators performing worse than the expert input. Thus, these runs were not investigated further. The runs with initial values at the maximum of the value range showed mixed performance. The run with *epsfcn*=0.1 performed worse than the expert input, while the run with *epsfcn*=0.25 showed values closer to those of the runs with minimum initial values.

The distributions of the $AUC$ values per plot for the best-performing optimisation runs for the initial values (A) minimum, (B) maximum, and (D) expert input are very similar to the distribution of the initial expert input (see Fig. 5). For runs (A) and (B), the optimised distributions differ significantly from those for the respective initial values, demonstrating

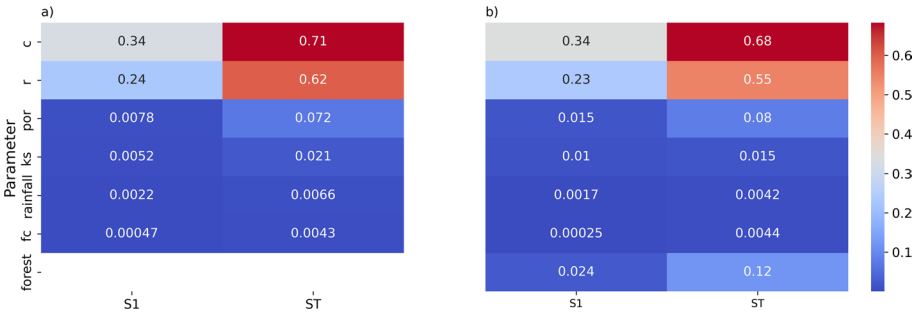


**Fig. 4** Heatmap showing the aggregated Sobol first-order (S1) and total-order (ST) indices for **a** the general analysis with six parameters using all 608 plots and **b** the analysis with an additional forest parameter using the 214 plots with at least 50% forest cover

**Table 4** Summary of the results of selected optimisation runs, including the number of function evaluations before stopping the optimisation; the Akaike Info Criterion (AIC); the Bayesian Info Criterion (BIC); the sum of $1 - AUC$; and the sum of $AUC$

| Run | Function evaluations | AIC | BIC | Sum $1 (-AUC)$ | Sum $(AUC)$ |
|---|---|---|---|---|---|
| Expert input, initial values | – | −1718.80 | −1657.56 | 557.22 | 658.78 |
| Expert input, *epsfcn*= default | 50 | −1718.80 | −1657.56 | 557.22 | 658.78 |
| Expert input, *epsfcn*=0.1 | 90 | −1745.72 | −1684.48 | 555.42 | 660.58 |
| Expert input, *epsfcn*=0.25 | 116 | −1747.02 | −1685.78 | 558.08 | 657.92 |
| Expert input, *epsfcn*=0.5 | 156 | −1747.68 | −1686.44 | 557.03 | 658.97 |
| Expert input, *epsfcn*=0.75 | 127 | −1746.71 | −1685.47 | 558.03 | 657.97 |
| Minimum initial, *epsfcn*=0.1 | 117 | −1772.29 | −1711.05 | 538.91 | 677.09 |
| Minimum initial, *epsfcn*=0.25 | 103 | −1773.32 | −1712.08 | 543.00 | 673.00 |
| Middle initial, *epsfcn*=0.25 | 142 | −1707.76 | −1646.52 | 584.12 | 631.88 |
| Maximum initial, *epsfcn*=0.1 | 88 | −1705.12 | −1643.88 | 569.57 | 646.43 |
| Maximum initial, *epsfcn*=0.25 | 152 | −1757.23 | −1695.99 | 546.36 | 669.64 |

clear improvements through optimisation (see A6). Run (C) for the middle initial values shows a significantly different distribution compared to the initial expert input. The values are almost normally distributed around the median of 0.5, with little difference between the initial and optimised distributions. For runs (A), (B), and (D), as well as for the initial expert input, the median across all plots (i.e. both with and without landslides) is close to 0.5, with a slight skew towards the value of 1. For run (D), the optimisation actually shifts the values a little closer to the median, which explains the slightly lower *Sum*(*AUC*). The optimised distributions for the plots without landslides for the runs (A), (B), and (D) show stronger concentrations around the median of 0.5, with slight skews towards 0. For the expert input, the optimised run shows a distribution similar to the initial values, but with a stronger concentration around the median of 0.5. The most notable differences are seen in the distributions for the plots with observed landslides. Runs (A) and (B) show a slightly higher median than the expert input, with a shift in the distribution towards 1. For run (D),

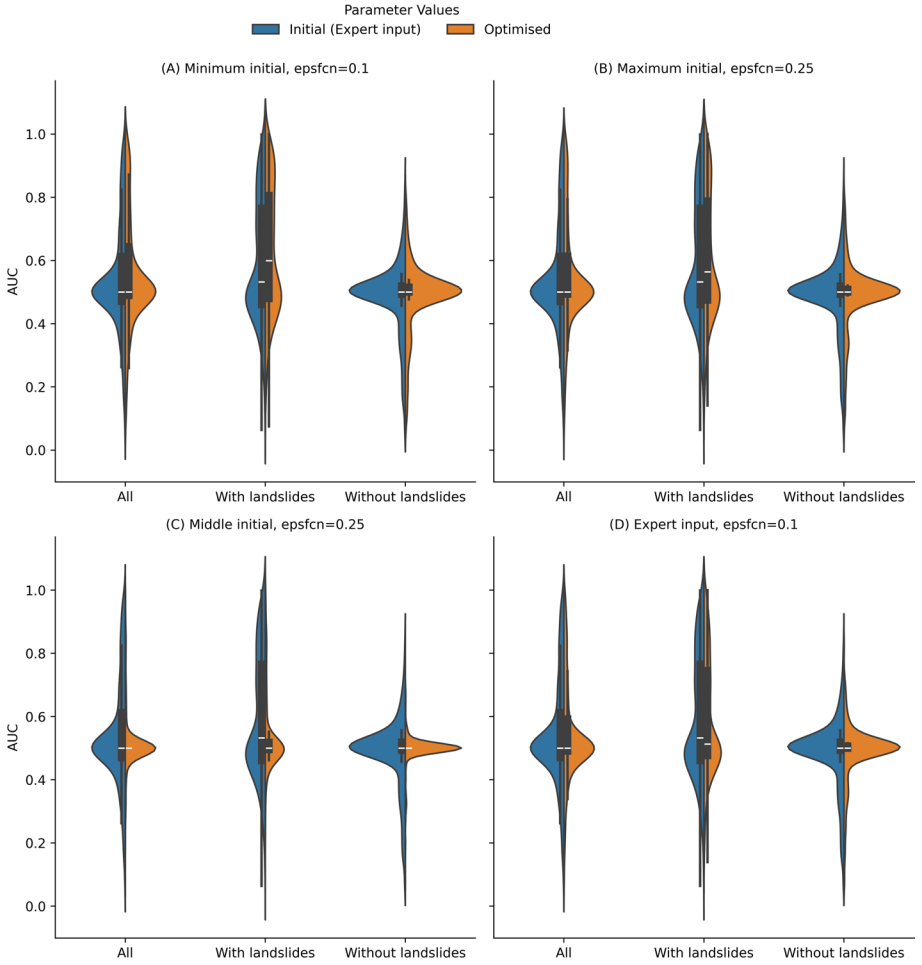


**Fig. 5** Split violin plots showing the distribution of the *AUC* over the hectare plots for the expert input values in blue vs. the optimised values for selected variants in orange, grouped according to the presence of observed landslides in the plot. The "All" group includes both plots with and without observed landslides

the initial expert input has a slightly higher median value than the optimisation, which shifts the median closer to 0.5 and the distribution slightly further away from 0.

Examining the parameter values for the selected runs (see Fig. 6) reveals clear differences despite similar *Sum*(*AUC*) values for the overall results and similar distributions of the *AUC* per plots. The value of the mean hydraulic conductivity shows a high variance compared to the expert input, with no clear trend as to whether the values are higher or lower than the input. The values for run (B) tend to stay close to the initial maximum value. The mean cohesion values for all soil classes tend to be higher than the expert input values, suggesting that higher values improve the result. The angle of internal friction values for soil classes 3 and 4 tend to be lower than the expert input, while those for soil classes 7 and 8 show no clear tendency. However, the values for runs (A) and (C) for the more common soil class 8 are close to the expert input, whereas the other two are spread towards the minimum and maximum of the value range. This suggests that the expert input may represent a reasonable midpoint.

### 5.3 Application of methodology at catchment scale

Examining the overall *AUC* values (Table 5) and plots of the ROC *AUC* curves (see Fig. A7), parametrisation (A), which is based on the optimisation with minimum initial values, shows the best overall performance of the four selected parametrisations. The only exception is the catchment in the Jura, where parametrisation (E), based on the initial expert input, performed best. The results for parametrisation (B), which uses optimised values based on the maximum initial values, are close to, but slightly lower than, those for parametrisation

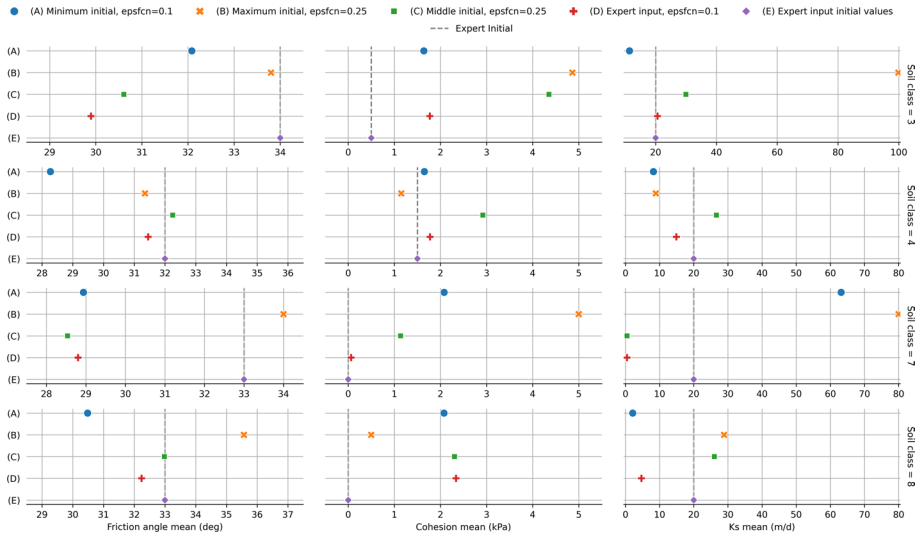


**Fig. 6** Visualisation of parameter values for the mean angle of internal friction, mean cohesion, and mean hydraulic conductivity (Ks) resulting from selected optimisation runs. The initial expert input is shown as a dashed line for comparison. The different points represent the tested optimisations: **A** Minimum initial, *epsfcn* = 0.1 (blue dot); **B** maximum initial, *epsfcn* = 0.25 (orange x); **C** middle initial, *epsfcn* = 0.25 (green square); **D** expert input, *epsfcn* = 0.1(red cross); and **E** expert input, initial values (violet rhombus). The value ranges of the x-axes correspond to the bounds used in the optimisation

(A). The results for parametrisation (D) with the optimised expert input tend to be slightly worse than those for parametrisation (E), except for the catchment in the Central Plateau.

At a cell size of 2 m, the spatial distribution of the absolute landslide occurrence probability shows higher probabilities in steeper terrain, in areas of water accumulation, and in the vicinity of historically observed landslides. However, at this cell size, the values mostly correspond to low to very low return periods (>1000 years), and the distribution is too fragmented for practical assessment. The aggregated occurrence probabilities at a 100 m cell size show plausible return periods (i.e. the reciprocal value of the occurrence probability, which corresponds to the average time between two events), and the distribution mostly agrees with the observed landslides (see Fig. 7). An exception is the catchment located in the Jura, where few landslides have been recorded. Within the same catchment, the spatial distribution and return periods differ slightly between the different parametrisations (see A.7).

When comparing the distribution of observed and aggregated landslide occurrence probabilities with a cell size of 100 m, the values corrected using the catchment as the reference area perform best overall (Fig. 8). Although the values show considerable variance, there is a general tendency towards underestimation. Values corrected using microcatchments as the reference area tend to result in overestimation. Corrections based on the hectare grid were not investigated further due to a pronounced tendency towards underestimation.

## 6 Discussion

### 6.1 Sensitivity results

The global sensitivity analysis indicated that mean cohesion and the angle of internal friction were the most sensitive among the investigated SFM parameters. This outcome aligns with the results of a sensitivity analysis performed by van Zadelhoff et al. (2022), who identified soil thickness as the most sensitive parameter, followed by cohesion and the angle of internal friction. However, we did not include soil thickness as a parameter, as this was fixed by the input raster. Van Zadelhoff et al. (2022) also identified hydraulic conductivity as a parameter with considerable sensitivity, which is consistent with our findings, where it was ranked as the fourth most sensitive parameter. The high sensitivity of SFM to vegetation in forested plots, parametrised by the individually detected trees, is likewise consistent with the findings of van Zadelhoff et al. (2022). Kuriakose et al. (2009) also reported that root cohesion, soil thickness, and angle of internal friction were the most influential parameters

**Table 5** AUC values calculated using the observed historical landslides for the application of four different sets of soil physical property parameters in the four selected catchments

| Catchment | Jura | Central plateau | Pre-Alps | Alps |
|---|---|---|---|---|
| *Simulation* | | | | |
| (A) Minimum initial optimised, *epsfcn* = 0.1 | 0.680 | 0.805 | 0.813 | 0.822 |
| (B) Maximum initial optimised, *epsfcn* = 0.25 | 0.630 | 0.778 | 0.808 | 0.814 |
| (D) Expert input optimised, *epsfcn* = 0.1 | 0.587 | 0.745 | 0.768 | 0.793 |
| (E) Expert input initial values | 0.730 | 0.733 | 0.780 | 0.794 |

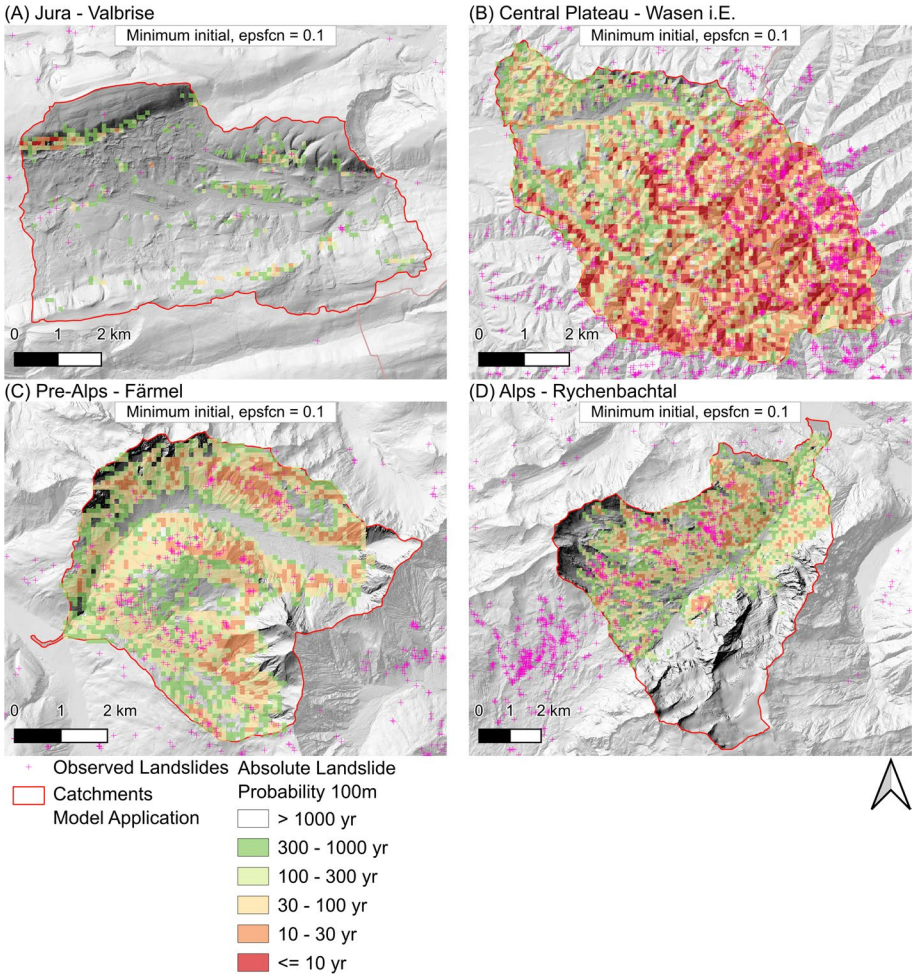


**Fig. 7** Maps presenting the return periods derived from the absolute landslide occurrence probability aggregated to 100 m cell size in the four catchments in **A** the Jura, **B** Central Plateau, **C** Pre-Alps, and **D** Alps for parametrisation based on the optimisation using minimum initial values and using the whole catchment as reference area for calculating the correction factor

affecting slope stability in a study that used a physically based, dynamic, and distributed hydrological model applied to the upper Tikovil River basin (55.6 $\mathrm{km}^2$) in Kerala, India.

The interaction between the cohesion and angle of internal friction parameters can be attributed to their roles in SFM. Each parameter contributes, through two different terms, to the basal component of the resisting force used to calculate the factor of safety (cf. equations 3 and 4 in van Zadelhoff et al. 2022). Basal and lateral root reinforcement contribute to the resisting force as well, which explains the low but noticeable interaction of the forest parameter and the two soil parameters.

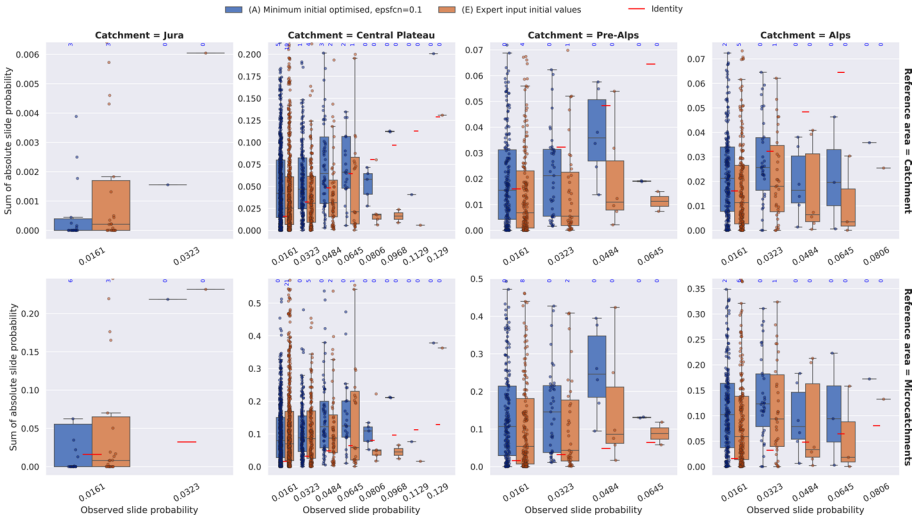


**Fig. 8** Box plot showing the observed vs. the sum of simulated landslide occurrence probabilities per catchment for variant (A) with the optimisation result based on the minimum initial values and (E) the initial expert input values. Values in the top row have been corrected using the entire catchment as the reference area, while values in the bottom row have been corrected using the most active microcatchment as the reference area. Red lines indicate the 1:1 point. Blue text indicates the number of outliers outside the plots' display range

## 6.2 Soil physical property optimisation

Optimisation is widely used in landslide modelling to improve model performance; for example, by optimising thresholds, selecting parameters, training models, or tuning hyperparameters of machine learning models (Merghadi et al. 2020; Liu et al. 2021; Ado et al. 2022; Greco et al. 2023). The Levenberg-Marquardt (LM) and its variants, such as the Gaus-Marquardt-Levenberg algorithm, are commonly applied to optimisation problems in this field (e.g. Min and Yoon 2021; Aaron et al. 2019). In our study, optimising parameters using the LM algorithm proved to be a viable approach. The best-performing optimised parameter sets and the initial expert input for the parameters yielded comparable overall results. This suggests that, given reasonable default values, the optimisation procedure can produce valid parameter sets for SFM simulations. It also confirms that the initial expert input is a viable parametrisation.

However, the optimisation process does have limitations. The observation that different initial values and configurations for the optimisation resulted in multiple parametrisations with similar performance but different parameter values (a condition called equifinality) leads us to conclude that the optimisation space contains multiple local minima. One possible cause is the spatial heterogeneity of soil classes, which is not captured by the parametrisation, where each soil class is assigned the same physical properties across the entire canton. Regional differentiation of soil properties could help address this issue, but would also increase the complexity of the optimisation procedure. Another potential cause lies in the plot selection procedure. Although the distribution of soil classes is similar in plots with and without observed landslides, the results suggest that the improvement in overall

performance is mainly due to improvements in the plots with observed landslides. Calculating the $AUC$ of the value $1 - failure\_probability$ for randomly generated points may not adequately represent the absence of landslides in the overall objective function. Including additional landslide absence data could improve the performance of landslide susceptibility models, but the availability and quality of absence data are often limited (Zhu et al. 2018). Refining the inputs for landslide absence and/or modifying the objective function could address this issue.

### 6.3 Application at catchment scale

The $AUC$ values for our regional application range from 0.59 to 0.82. These largely fall within the range of 0.64 to 0.93 reported by van Zadelhoff et al. (2022) for SFM simulations with a number of different parametrisations in three test areas in Switzerland. Cislaghi et al. (2018) reported an $AUC$ value of 0.832 for their PRIMULA model (which has close similarities to SFM) in the Rio Davedino catchment (8.69 $\mathrm{km}^2$) in the south-eastern Italian Alps. Our three optimised parametrisations and the expert input performed equally well in the three catchments in the Central Plateau, the pre-Alps and the Alps. However, the performance in the catchment located in the Jura was worse than that of the expert input. This shows that the parametrisations perform well on average across the canton, but that local variability exists. It may also reflect the challenges associated with catchments that have few or no observed landslides, which are likely linked to the previously discussed issues with optimisation in plots lacking landslide observations.

The occurrence probabilities resulting from the application, when aggregated to a 100 m cell size, generally show plausible values. However, the choice of the reference area used to calculate the correction factor to normalise the relative probabilities to the actual occurrence of landslides in the observation period has a significant impact on the outcome. Using the most active hectare for the correction leads to clear overestimation. Using the most active microcatchment tends to slightly overestimate, while using the entire 40 $\mathrm{km}^2$ catchment tends to slightly underestimate. However, care must be taken when interpreting the results, as the correction factor and, consequently, the results also depend on the quality and completeness of the landslide inventory used. In catchments with a sufficient number of observed landslides, results corrected, based on either the entire catchment or the microcatchment, can be readily used for practical applications, such as the creation of hazard indication maps. However, the results in the Jura catchment show that caution is required in areas with few or no observed landslides, as the resulting correction factors tend to significantly underestimate landslide occurrence probabilities.

The developed methodology can be used for applications in other areas. The availability of the required input data may limit the direct transfer, but alternate input data (e.g. for the soil classes or forest structure) may be substituted. The estimation of shallow landslide occurrence probability by combining and normalising relative values depends strongly on the completeness of datasets with historical landslide events, but can be used for different types of slope stability models. Finally, the parameter optimisation can be adapted for other parameters and/or models.

### 6.4 Uncertainty

Despite considerable parametric and predictive uncertainty, the results of our methodology appear promising. Factors contributing to uncertainty in landslide susceptibility models include: (1) the type, availability, and reliability of the input data; (2) the spatial variability in geotechnical and hydrological parameters; (3) the uncertainty in the classification of individual mapping units; and (4) the uncertainty in the model outputs and their geographical distribution (Guzzetti et al. 2006; Reichenbach et al. 2018; Oguz et al. 2022). In their review of 565 peer-reviewed articles on statistical methods for landslide susceptibility from 1983 to 2016, Reichenbach et al. (2018) reported that authors only started to perform uncertainty analysis after 2000, and then only in 3% of the articles. In this study, we did not apply uncertainty quantification due to the inherent difficulties in quantifying uncertainty in the model as well as in the reference and input data. In particular, some of the input data are based on different machine learning models, for which there are no universally applicable solutions for measuring uncertainty (Jalaian et al. 2019; Simmonds et al. 2022). These data represent a significant source of uncertainty, as inaccuracies in the inputs propagate through the models and ultimately affect the predictions (Simmonds et al. 2022).

Despite similar overall *AUC* values, different parametrisations show differences in the absolute landslide probability within the same catchment. This illustrates the spatial uncertainty in the model outputs resulting from the different inputs and their associated uncertainties. This confirms that, while the *AUC* can capture the overall validity of the results, it cannot capture the spatially dependent uncertainty (Vakhshoori and Zare 2018).

The main sources of uncertainty in the input data are soil classes and their physical properties, as well as the landslide thickness. Maps of soil thickness and properties are subject to high uncertainty due to the often sparse field measurements, low mapping resolution, and the large heterogeneity in soil variables (Cohen et al. 2009; Jia et al. 2012; Lanni et al. 2012). The predicted landslide thickness is based on a random forests-based ML model that was trained using a landslide inventory and a number of covariates, including a terrain model, canopy height model, and information on the geological substratum (Schaller et al. 2025). Both the input data and the overall model are subject to uncertainties that have not been quantified (Schaller et al. 2025). The soil property maps used to define the soil classes were predicted using quantile regression forest (Meinshausen 2006) based on sparse field measurements and a large number of covariates derived from remote sensing (Stumpf et al. 2024). The 30 m cell size of the soil property maps and their mapping to the soil classes used in this study introduces a degree of simplification. Additionally, the selection of the parameter values for soil physical properties only represents one possible value for the average properties of each soil class. Sensitivity analysis and optimisation also showed that different combinations of parameter values (particularly mean cohesion and mean angle of internal friction) can result in similar outputs due to the structure of the model. Correctly estimating the hydraulic conductivity is also challenging because the macropore structure, which significantly influences the conductivity, can be highly heterogeneous (e.g. due to the root systems of different types of vegetation) (Murgia et al. 2022; van Zadelhoff et al. 2022; Greco et al. 2023). Furthermore, the lack of data in areas assumed to have no soil cover is problematic, as 12% of the landslides in the landslide inventory used (Hählen 2024) are in the *NoSlide* soil class. This is particularly the case at the edges of areas such as water bodies, settlements, and bare rock. Using regionally differentiated soil classes in combination with

optimisation could address some of these issues, thereby reducing uncertainty and improving the overall performance of the model.

Hydrological uncertainties are largely determined by hydrological model implemented in SFM and the rainfall scenarios used as input. SFM models hydrology based on the TOPOG model (O'Loughlin 1986), which includes a topographic index inspired by Kirkby (1975). The model specifically assumes that macropore flow dominates hillslope hydrology (van Zadelhoff et al. 2022). Therefore, SFM only considers surface hydrology. Local factors influencing soil moisture and water pressure, such as local springs or rising groundwater, are not considered. We have not matched the observed landslides with historical events and therefore do not take into account the scenarios that lead to specific landslides. Our approach attempts to mitigate this by combining the relative susceptibility values from simulations for rainfall scenarios with different return periods. The rainfall amounts used to parametrise the simulations are based on statistically modelled extreme point precipitation scenarios (Frei and Fukutome 2022). These are subject to uncertainty, which is reflected in the availability of rainfall values for different confidence intervals. The use of an average rainfall value for the entire catchment area without considering local variations (e.g. due to different topography) adds to this uncertainty. We plan to address this issue in SFM by including the possibility to use spatially differentiated rainfall rasters.

The forest structure input data, including tree positions, DBH, and species, significantly influences the landslide probability calculated by SFM within forest covered areas (van Zadelhoff et al. 2022). Although we used individual tree data resulting from a local maxima approach that optimises detection using an ML model based on forest structure (Schaller et al. 2023), the data only include the (co-)dominant trees. In addition, the actual position on the ground may differ from the detected position of the crown, and DBH is calculated using a general allometric function fitted to inventory data. Furthermore, the actual forest structure may have changed since the acquisition of the CHM. Using a single tree species per plot or catchment is also subject to considerable uncertainty. The forest data on the coniferous proportion, which was used to select the species, are subject to uncertainty, as they were modelled using random forests and neuronal networks with remotely sensed data (Waser et al. 2017). In particular, the data underestimate broadleaf trees due to errors in the input image data (Waser et al. 2017). An alternative approach to species parametrisation would be to probabilistically assign species to the individual trees based on the coniferous proportion.

The possible error of 10-25% in the size of the landslides estimated by Hählen (2023) affects the uncertainty of the relative landslide probabilities, as the size is used to parametrise the inverse gamma distribution that determines the area of the hypothetical landslides in SFM (van Zadelhoff et al. 2022). The completeness of events in the inventory directly influences the parameter optimisation, the correction factor for the absolute occurrence probability, and the calculation of the $AUC$ used to measure performance. The absence of events in a particular area does not exclude the possibility of a landslide. There may simply not have been an event within the observation period, or an event may not have been recorded. Events in forested or intensively cultivated areas may not be visible in the orthoimagery used for the inventory (Hählen 2023). In addition, the 62-year observation period also influences uncertainty. Significant changes in the landscape may have occurred between the recorded landslide and the current input data used for the simulations, e.g. in settlement areas or locations where the landslides denuded the entire slope, preventing new landslides from occurring for the foreseeable future. Continuous improvements in soil

mapping and modelling methods, inventory methods, and ML methods will contribute to a reduction of these uncertainties in the future.

## 7 Conclusion

We developed a methodology for assessing shallow landslide susceptibility at regional scale based on slope stability simulations using SFM. A global sensitivity analysis revealed that mean cohesion, angle of internal friction, and forest effect were the most important model parameters. Using soil property maps as input provides a standardised approach to defining soil classes. However, parameter equifinality suggests that the parametrisation does not adequately represent the heterogeneity and local variability in the soil classes' physical properties. The application at catchment scale demonstrates that the optimisation approach has the potential to yield suitable parameters that produce results comparable to those obtained using expert input. Despite certain limitations, the catchment-scale application produced plausible results. We consider our methodology to be a viable alternative for generating information for practical applications such as regional-scale hazard indication mapping.

**Supplementary Information** The online version contains supplementary material available at https://doi.org/10.1007/s11069-025-07701-6.

**Author contributions** Christoph Schaller: Conceptualisation, Methodology, Software, Validation, Formal analysis, Investigation, Resources, Data Curation, Writing—Original Draft, Writing—Review & Editing, Visualisation. Denis Cohen: Conceptualisation, Methodology, Software, Writing—Original Draft, Writing—Review & Editing. Arie C. Seijmonsbergen: Writing—Review & Editing, Supervision. Luuk Dorren: Conceptualisation, Methodology, Software, Writing—Original Draft, Writing—Review & Editing, Supervision, Project administration, Funding acquisition. Emiel van Loon: Methodology, Writing—Review & Editing, Supervision.

**Funding** Open access funding provided by Bern University of Applied Sciences. This research has been supported by internal PhD funding from the Bern University of Applied Sciences and by the Principality of Liechtenstein (grant name: RHK Rutsch FL).

**Data availability** Code for this study and data for replicating the analysis are published on Zenodo: https://doi.org/10.5281/zenodo.17091608 (Schaller 2025).

## Declarations

**Conflict of interest** The authors declare that they have no known competing financial interests or personal relationships that could have appeared to influence the work reported in this paper.

## References


Ado M, Amitab K, Maji AK, Jasińska E, Gono R, Leonowicz Z, Jasiński M (2022) Landslide susceptibility mapping using machine learning: a literature survey. Remote Sens 14(13):3029. https://doi.org/10.3390/rs14133029

Alaoui A, Caduff U, Gerke Hh, Weingartner R (2011) Preferential flow effects on infiltration and Runoff in grassland and forest soils. Vadose Zone J 10(1):367–377. https://doi.org/10.2136/vzj2010.0076

Ali A, Huang J, Lyamin AV, Sloan SW, Griffiths DV, Cassidy MJ, Li JH (2014) Simplified quantitative risk assessment of rainfall-induced landslides modelled by infinite slopes. Eng Geol 179:102–116. https://doi.org/10.1016/j.enggeo.2014.06.024

Aaron J, McDougall S, Nolde N (2019) Two methodologies to calibrate landslide runout models. Landslides 16(5):907–920. https://doi.org/10.1007/s10346-018-1116-8

BAFU (2019) Topographische Einzugsgebiete Schweizer Gewässer Schweiz, Ausgabe 2019. Bundesamt für Umwelt https://data.geo.admin.ch/ch.bafu.wasser-teileinzugsgebiete_2/ Accessed 2023-07-26

BAFU B (2024) Indikator Naturgefahren. https://www.bafu.admin.ch/bafu/de/home/themen/thema-naturgefahren/naturgefahren--daten--indikatoren-und-karten/naturgefahren--indikatoren/indikator-naturgefahren.html. Accessed 2025-04-23

Badoux A, Andres N, Techel F, Hegg C (2016) Natural hazard fatalities in switzerland from 1946 to 2015. Nat Hazard Earth Sys 16(12):2747–2768. https://doi.org/10.5194/nhess-16-2747-2016

Baum RL, Savage WZ, Godt JW (2002) TRIGRS - a Fortran program for transient rainfall infiltration and grid-based regional slope-stability analysis. Open-File Report. https://doi.org/10.3133/ofr02424. Accessed 2024-01-31

Caine N (1980) The rainfall intensity - duration control of shallow landslides and debris flows. Geogr Ann A Phys Geogr 62(1–2):23–27. https://doi.org/10.1080/04353676.1980.11879996

Conrad O, Bechtel B, Bock M, Dietrich H, Fischer E, Gerlitz L, Wehberg J, Wichmann V, Böhner J (2015) System for Automated Geoscientific Analyses (SAGA) v. 2.1.4. Geosci. Model Dev 8(7), 1991–2007. https://doi.org/10.5194/gmd-8-1991-2015

Chirico GB, Borga M, Tarolli P, Rigon R, Preti F (2013) Role of vegetation on slope stability under transient unsaturated conditions. Procedia Environ Sci 19:932–941. https://doi.org/10.1016/j.proenv.2013.06.103

CCSol (2024) Swiss competence center for soils home page. https://ccsols.ch/de/home/. Accessed 2024-08-16

Cohen D, Lehmann P, Or D (2009) Fiber bundle model for multiscale modeling of hydromechanical triggering of shallow landslides. Water Resour Res. https://doi.org/10.1029/2009WR007889

Cislaghi A, Rigon E, Lenzi MA, Bischetti GB (2018) A probabilistic multidimensional approach to quantify large wood recruitment from hillslopes in mountainous-forested catchments. Geomorphology 306:108–127. https://doi.org/10.1016/j.geomorph.2018.01.009

Cohen D, Schwarz M (2017) Tree-root control of shallow landslides. Earth Surf Dyn 5(3) 451–477. https://doi.org/10.5194/esurf-5-451-2017. Publisher: Copernicus GmbH

Chandler KR, Stevens CJ, Binley A, Keith AM (2018) Influence of tree species and forest land use on soil hydraulic conductivity and implications for surface runoff generation. Geoderma 310:120–127. https://doi.org/10.1016/j.geoderma.2017.08.011

Catani F, Segoni S, Falorni G (2010) An empirical geomorphology-based approach to the spatial prediction of soil thickness at catchment scale. Water Resour Res. https://doi.org/10.1029/2008WR007450

Chinkulkijniwat A, Tirametatiparat T, Supotayan C, Yubonchit S, Horpibulsuk S, Salee R, Voottipruex P (2019) Stability characteristics of shallow landslide triggered by rainfall. J Mt Sci 16(9):2171–2183. https://doi.org/10.1007/s11629-019-5523-7

Cruden D, Varnes DJ (1996) Landslide Types and Processes. In: Turner AK, Schuster RL (eds), Landslides: investigation and mitigation. National Academy Press, Washington, vol 247, pp 36–75

DiBiagio A, Capobianco V, Oen A, Tallaksen LM (2024) State-of-the-art: parametrization of hydrological and mechanical reinforcement effects of vegetation in slope stability models for shallow landslides. Landslides 21(10):2417–2446. https://doi.org/10.1007/s10346-024-02300-1

Dazio EPR, Conedera M, Schwarz M (2018) Impact of different chestnut coppice managements on root reinforcement and shallow landslide susceptibility. For Ecol Manag 417:63–76. https://doi.org/10.1016/j.foreco.2018.02.031

Dahl M-PJ, Mortensen LE, Veihe A, Jensen NH (2010) A simple qualitative approach for mapping regional landslide susceptibility in the Faroe islands. Nat Hazard Earth Sys 10(2):159–170. https://doi.org/10.5194/nhess-10-159-2010

Di Napoli M, Di Martire D, Bausilio G, Calcaterra D, Confuorto P, Firpo M, Pepe G, Cevasco A (2021) Rainfall-induced shallow landslide detachment, transit and runout susceptibility mapping by integrating machine learning techniques and GIS-based approaches. Water 13(4) 488. https://doi.org/10.3390/w13040488. Accessed 2024-02-01

Dysli M, Rybisar J (1992) Statistique sur les caractéristiques des sols suisses - Statistische Behandlung der Kennwerte der Schweizer Böden. Technical report, Bundesamt für Strassenbau, Institut Francais des Sciences et Technologies des Transports, de l'Aménagement et des Réseaux (IFSTTAR). https://www.mobilityplatform.ch/de/244.html Accessed 2025-07-30

Emberson R, Kirschbaum D, Stanley T (2020) New global characterisation of landslide exposure. Nat Hazard Earth Sys 20(12):3413–3424. https://doi.org/10.5194/nhess-20-3413-2020

Ester M, Kriegel H-P, Sander J, Xu X (1996) A density-based algorithm for discovering clusters in large spatial databases with noise. In: Proceedings of the 2nd international conference on knowledge discovery and data mining. KDD'96, pp. 226–231. AAAI Press, Portland, Oregon. http://www.aaai.org/Papers/KDD/1996/KDD96-037.pdf Accessed 2025-04-25

Fallot J-M (2021) Climate setting in Switzerland. In: Reynard E (ed) Landscapes and Landforms of Switzerland, Springer, Cham, pp 31–45. https://doi.org/10.1007/978-3-030-43203-4_3

Fawcett T (2006) An introduction to roc analysis. Pattern Recognit Lett 27(8):861–874. https://doi.org/10.1016/j.patrec.2005.10.010

Frei C, Fukutome S (2022) Extreme Point Precipitation. In: Weingartner R, Hauser F (eds) Data and analysis platform. hydrological atlas of Switzerland, Bern. https://hydromaps.ch/#en/8/46.830/8.190/bl_hds--precip_24h_2a$4/NULL Accessed 2023-06-12

Froude MJ, Petley DN (2018) Global fatal landslide occurrence from 2004 to 2016. Nat Hazards Earth Syst Sci 18(8):2161–2181. https://doi.org/10.5194/nhess-18-2161-2018

FSO (2024) Swiss Land Use Statistics: standard nomenclature (NOAS04) by major region and canton, in hectares. Federal Statistical Office. https://www.bfs.admin.ch/asset/en/32267652 Accessed 2025-05-01

Guzzetti F, Carrara A, Cardinali M, Reichenbach P (1999) Landslide hazard evaluation: a review of current techniques and their application in a multi-scale study. Central Italy Geomorphol 31(1):181–216. https://doi.org/10.1016/S0169-555X(99)00078-1

Gehring E, Conedera M, Maringer J, Giadrossich F, Guastini E, Schwarz M (2019) Shallow landslide disposition in burnt European beech (Fagus sylvatica L.) forests. Sci Rep 9(1):8638. https://doi.org/10.1038/s41598-019-45073-7

GDAL/OGR contributors: GDAL/OGR Geospatial Data Abstraction software Library (2021). https://gdal.org

García-Gaines RA, Frankenstein S (2015) USCS and the USDA soil classification system: Development of a mapping scheme. https://doi.org/10.21236/ADA614144. Publisher: Cold Regions Research and Engineering Laboratory (US)

Gamboa F, Janon A, Klein T, Lagnoux A (2013) Sensitivity indices for multivariate outputs. C R Math 351(7):307–310. https://doi.org/10.1016/j.crma.2013.04.016

Greco R, Marino P, Bogaard TA (2023) Recent advancements of landslide hydrology. WIREs Water 10(6):1675. https://doi.org/10.1002/wat2.1675

Guzzetti F, Peruccacci S, Rossi M, Stark CP (2008) The rainfall intensity-duration control of shallow landslides and debris flows: an update. Landslides 5(1):3–17. https://doi.org/10.1007/s10346-007-0112-1

Guzzetti F, Reichenbach P, Ardizzone F, Cardinali M, Galli M (2006) Estimating the quality of landslide susceptibility models. Geomorphology 81(1):166–184. https://doi.org/10.1016/j.geomorph.2006.04.007

Greenway DR (1987) Vegetation and slope stability. In: Anderson MG, Richards KS (eds) Slope stabilization. Wiley, New York, pp 187–223

Horton P, Jaboyedoff M, Rudaz B, Zimmermann M (2013) Flow-r, a model for susceptibility mapping of debris flows and other gravitational hazards at a regional scale. Nat Hazard Earth Sys 13(4):869–885. https://doi.org/10.5194/nhess-13-869-2013

Hungr O, Leroueil S, Picarelli L (2014) The varnes classification of landslide types, an update. Landslides 11(2):167–194. https://doi.org/10.1007/s10346-013-0436-y

Hengl T, Jesus J, Heuvelink GBM, Ruiperez Gonzalez M, Kilibarda M, Blagotić A, Shangguan W, Wright MN, Geng X, Bauer-Marschallinger B, Guevara MA, Vargas R, MacMillan RA, Batjes NH, Leenaars JGB, Ribeiro E, Wheeler I, Mantel S, Kempen B (2017) SoilGrids250m: Global gridded soil information based on machine learning. PLOS ONE 12(2):0169748. https://doi.org/10.1371/journal.pone.0169748

Herman J, Usher W (2017) Salib: an open-source python library for sensitivity analysis. J Open Source Softw 2(9):97. https://doi.org/10.21105/joss.00097

Hählen, N (2023) Kennzahlen zu Spontanen Rutschungen Im Kanton Bern Mit Schwerpunkt Auf Alpen Und Voralpen. https://www.researchgate.net/publication/368510037

Hählen, N.: Orthofotobasiertes Inventar spontaner, flachgründiger Rutschungen im Kanton Bern (2024). https://researchgate.net/publication/384051894_Orthofotobasiertes_Inventar_spontaner_flachgrundiger_Rutschungen_im_Kanton_Bern. Accessed 28 Apr 2025

Iverson RM (2000) Landslide triggering by rain infiltration. Water Resour Res 36(7):1897–1910. https://doi.org/10.1029/2000WR900090

Jalaian B, Lee M, Russell S (2019) Uncertain context: uncertainty quantification in machine learning. AI Mag 40(4):40–49. https://doi.org/10.1609/aimag.v40i4.4812
Jia N, Mitani Y, Xie M, Djamaluddin I (2012) Shallow landslide hazard assessment using a three-dimensional deterministic model in a mountainous area. Comput Geotech 45:1–10. https://doi.org/10.1016/j.compgeo.2012.04.007
Kaur H, Gupta S, Parkash S, Thapa R, Gupta A, Khanal GC (2019) Evaluation of landslide susceptibility in a hill city of sikkim himalaya with the perspective of hybrid modelling techniques. Ann GIS 25(2):113–132. https://doi.org/10.1080/19475683.2019.1575906
Kirkby M (1975) Hydrograph modelling strategies. In: Peel R, Chisholm M, Haggert P (eds) Process in physical and human geography. Heineman, London, pp 69–90
Kuriakose SL, Beek LPH, Westen CJ (2009) Parameterizing a physically based shallow landslide model in a data poor region. Earth Surf Proc Land 34(6):867–881. https://doi.org/10.1002/esp.1794
Lanni C, Borga M, Rigon R, Tarolli P (2012) Modelling shallow landslide susceptibility by means of a subsurface flow path connectivity index and estimates of soil depth spatial distribution. Hydrol Earth Ssyst Sc 16(11):3959–3971. https://doi.org/10.5194/hess-16-3959-2012
Liu Z, Gilbert G, Cepeda JM, Lysdahl AOK, Piciullo L, Hefre H, Lacasse S (2021) Modelling of shallow landslides with machine learning algorithms. Geosci Front 12(1):385–393. https://doi.org/10.1016/j.gsf.2020.04.014
Lateltin O, Haemmig C, Raetzo H, Bonnard C (2005) Landslide risk management in Switzerland. Landslides 2(4):313–320. https://doi.org/10.1007/s10346-005-0018-8
Li WC, Lee LM, Cai H, Li HJ, Dai FC, Wang ML (2013) Combined roles of saturated permeability and rainfall characteristics on surficial failure of homogeneous soil slope. Eng Geol 153:105–113. https://doi.org/10.1016/j.enggeo.2012.11.017
Leonarduzzi E, Molnar P, McArdell BW (2017) Predictive performance of rainfall thresholds for shallow landslides in switzerland from gridded daily data. Water Resour Res 53(8):6612–6625. https://doi.org/10.1002/2017WR021044
Montgomery DR, Dietrich WE (1994) A physically based model for the topographic control on shallow landsliding. Water Resour Res 30(4):1153–1171. https://doi.org/10.1029/93WR02979
Meinshausen N (2006) Quantile regression forests. J Mach Learn Res 7(35):983–999
Metz CE (1978) Basic principles of roc analysis. Semin Nucl Med 8(4):283–298. https://doi.org/10.1016/S0001-2998(78)80014-2
Murgia I, Giadrossich F, Mao Z, Cohen D, Capra GF, Schwarz M (2022) Modeling shallow landslides and root reinforcement: a review. Ecol Eng 181:106671. https://doi.org/10.1016/j.ecoleng.2022.106671
May D, Markart G, Kohl B, Schwarz M (2024) Investigations on the effects of game browsing on surface runoff in Alpine forests. Research Square. https://doi.org/10.21203/rs.3.rs-5083736/v1. https://www.researchsquare.com/article/rs-5083736/v1 Accessed 2025-03-31
Moré, JJ (1978) The Levenberg-Marquardt algorithm: Implementation and theory. In: Watson GA (ed) Numerical analysis, Springer, Berlin, pp 105–116. https://doi.org/10.1007/BFb0067700
Masi EB, Segoni S, Tofani V (2021) Root reinforcement in slope stability models: a review. Geosci 11(5):212. https://doi.org/10.3390/geosciences11050212
Malamud BD, Turcotte DL, Guzzetti F, Reichenbach P (2004) Landslide inventories and their statistical properties. Earth Surf Proc Land 29(6):687–711. https://doi.org/10.1002/esp.1064
Min D-H, Yoon H-K (2021) Suggestion for a new deterministic model coupled with machine learning techniques for landslide susceptibility mapping. Sci Rep 11(1):6594. https://doi.org/10.1038/s41598-021-86137-x
Merghadi A, Yunus AP, Dou J, Whiteley J, ThaiPham B, Bui DT, Avtar R, Abderrahmane B (2020) Machine learning methods for landslide susceptibility studies: a comparative overview of algorithm performance. Earth-Sci Rev 207:103225. https://doi.org/10.1016/j.earscirev.2020.103225
Newville M, Otten R, Nelson A, Stensitzki T, Ingargiola A, Allan D, Fox A, Carter F, Michał, Osborn R, Pustakhod D, Weigand S, lneuhaus, Aristov A, Glenn, Mark, mgunyho, Deil C, Hansen ALR, Pasquevich G, Foks L, Zobrist N, Frost O, Stuermer, Jaskula J-C, Caldwell S, Eendebak P, Pompili M, Nielsen JH, Persaud A (2024) lmfit/lmfit-py: 1.3.2. Zenodo. https://doi.org/10.5281/zenodo.12785036
NRCS. (2024) Soil texture calculator: multi-point texture triangle excel version. U.S. Department of Agriculture - Natural Resources Conservation Service. https://www.nrcs.usda.gov/resources/education-and-teaching-materials/soil-texture-calculator Accessed 2024-09-03
Oguz EA, Depina I, Thakur V (2022) Effects of soil heterogeneity on susceptibility of shallow landslides. Landslides 19(1):67–83. https://doi.org/10.1007/s10346-021-01738-x
O'Loughlin EM (1986) Prediction of surface saturation zones in natural catchments by topographic analysis. Water Resour Res 22(5):794–804. https://doi.org/10.1029/WR022i005p00794
O'Callaghan JF, Mark DM (1984) The extraction of drainage networks from digital elevation data. Comput Gr Image Process 28(3):323–344. https://doi.org/10.1016/S0734-189X(84)80011-0

Piegari E, Cataudella V, Maio R, Milano L, Nicodemi M (2006) A cellular automaton for the factor of safety field in landslides modeling. Geophys Res Lett. https://doi.org/10.1029/2005GL024759

Pfiffner OA (2021) The geology of Switzerland. In: Reynard E (ed) Landscapes and landforms of Switzerland, Springer, Cham, pp 7–30. https://doi.org/10.1007/978-3-030-43203-4_2

Pack R, Tarboton D, Goodwin C (1998) The SINMAP approach to terrain stability mapping. In: Procedeengs of the 8th congress of the international association of engineering geology, Vancouver, pp 21–25

Pedregosa F, Varoquaux G, Gramfort A, Michel V, Thirion B, Grisel O, Blondel M, Prettenhofer P, Weiss R, Dubourg V, Vanderplas J, Passos A, Cournapeau D, Brucher M, Perrot M, Duchesnay E (2011) Scikit-learn: machine learning in python. J Mach Learn Res 12:2825–2830

R Core Team: R (2022) A language and environment for statistical computing. Place: Vienna. https://www.R-project.org/ Accessed 2025-05-13

Rickli C, Graf F, Bebi P, Bast A, Loup B, McArdell B (2019) Schützt der wald vor rutschungen? hinweise aus der wsl-rutschungsdatenbank. Schweiz Z Forstwes 170(6):310–317. https://doi.org/10.3188/szf.2019.0310

Rüegger R, Hufenus R (2003) Bauen Mit Geokunststoffen - Ein Handbuch Für Den Geokunststoff-Anwender. St. Gallen, Schweizerischer Verband für Geokunststoffe (SVG)

Reynard E, Häuselmann P, Jeannin P-Y, Scapozza C (2021) Geomorphological landscapes in Switzerland. In: Reynard E (ed) Landscapes and landforms of Switzerland. Springer, Cham, pp 71–80. https://doi.org/10.1007/978-3-030-43203-45

Ran Q, Hong Y, Li W, Gao J (2018) A modelling study of rainfall-induced shallow landslide mechanisms under different rainfall characteristics. J Hydrol 563:790–801. https://doi.org/10.1016/j.jhydrol.2018.06.040

Rickli C, McArdell B, Badoux A, Loup B (2016) Database shallow landslides and hillslope debris flows. 13th congress INTERPRAEVENT. 30 May to 2 June 2016. Lucerne, Switzerland. Extended abstracts "Living with natural risks", 242–243 (2016). Accessed 2023-05-01

Reichenbach P, Rossi M, Malamud BD, Mihir M, Guzzetti F (2018) A review of statistically-based landslide susceptibility models. Earth-Sci Rev 180:60–91. https://doi.org/10.1016/j.earscirev.2018.03.001

Saltelli A, Annoni P, Azzini I, Campolongo F, Ratto M, Tarantola S (2010) Variance based sensitivity analysis of model output: design and estimator for the total sensitivity index. Comput Phys Commun 181(2):259–270. https://doi.org/10.1016/j.cpc.2009.09.018

Simmonds EG, Adjei KP, Andersen CW, Hetle Aspheim JC, Battistin C, Bulso N, Christensen HM, Cretois B, Cubero R, Davidovich IA, Dickel L, Dunn B, Dunn-Sigouin E, Dyrstad K, Einum S, Giglio D, Gjerløw H, Godefroidt A, González-Gil R, Gonzalo Cogno S, Große F, Halloran P, Jensen MF, Kennedy JJ, Langsæther PE, Laverick JH, Lederberger D, Li C, Mandeville EG, Mandeville C, Moe E, Navarro Schröder T, Nunan D, Sicacha-Parada J, Simpson MR, Skarstein ES, Spensberger C, Stevens R, Subramanian AC, Svendsen L, Theisen OM, Watret C, O'Hara RB (2022) Insights into the quantification and reporting of model-related uncertainty across different disciplines. iScience 25(12):105512. https://doi.org/10.1016/j.isci.2022.105512

Saltelli A (2002) Making best use of model evaluations to compute sensitivity indices. Comput Phys Commun 145(2):280–297. https://doi.org/10.1016/S0010-4655(02)00280-1

Singh P, Bardhan A, Han F, Samui P, Zhang W (2023) A critical review of conventional and soft computing methods for slope stability analysis. Model Earth Syst Environ 9(1):1–17. https://doi.org/10.1007/s40808-022-01489-1

Stumpf F, Behrens T, Schmidt K, Keller A (2023) Hinweiskarten für bodeneigenschaften-landesweit modellierte karten für bodeneigenschaften für drei tiefenstufen. Technical Report 6, Kompetenzzentrum Boden (KOBO), ccsols.ch, Zollikofen (October). https://ccsols.ch/wp-content/uploads/2023/11/Hinweiskarten_Bodeneigenschaften_CH_final.pdf Accessed 2024-08-16

Stumpf F, Behrens T, Schmidt K, Keller A (2024) Exploiting soil and remote sensing data archives for 3d mapping of multiple soil properties at the swiss national scale. Remote Sens 16(15):2712. https://doi.org/10.3390/rs16152712

Schaller C (2025) HAFL-WWI/Landslide_Probability_Simulation: Release for Optimisation and application of shallow landslide model at regional scale v0.2. Zenodo. Version Number: SL_prob_sim_v0.2 . https://doi.org/10.5281/zenodo.17091608

Schaller C, Dorren L, Schwarz M, Moos C, Seijmonsbergen AC, Loon EE (2025) Predicting the thickness of shallow landslides in Switzerland using machine learning. Nat Hazards Earth Syst Sci 25(2):467–491. https://doi.org/10.5194/nhess-25-467-2025

Schaller C, Ginzler C, Loon E, Moos C, Seijmonsbergen AC, Dorren L (2023) Improving country-wide individual tree detection using local maxima methods based on statistically modeled forest structure information. Int J Appl Eearth Obs 123:103480. https://doi.org/10.1016/j.jag.2023.103480

Sobol' IM (2001) Global sensitivity indices for nonlinear mathematical models and their monte carlo estimates. Math Comput Simul 55(1):271–280. https://doi.org/10.1016/S0378-4754(00)00270-6

Schwarz M, Preti F, Giadrossich F, Lehmann P, Or D (2010) Quantifying the role of vegetation in slope stability: a case study in Tuscany (Italy). Ecol Eng 36(3):285–291. https://doi.org/10.1016/j.ecoleng.2009.06.014

Shano L, Raghuvanshi TK, Meten M (2020) Landslide susceptibility evaluation and hazard zonation techniques - a review. Geoenviron Disast 7(1):18. https://doi.org/10.1186/s40677-020-00152-0

Schuster R, Wieczorek G (2018) Landslide triggers and types. In: Landslides - proceedings of the first European conference on landslides, Prague, 24-26 June 2002, Routledge, pp 59–78. https://doi.org/10.1201/9780203749197-4

Swiss Re Institute (2019) Natural catastrophes and man-made disasters in 2018: secondary perils on the frontline. Sigma 2(2):1–36

Swisstopo (2023) swissALTI3D. Federal Office of Topography swisstopo. https://www.swisstopo.admin.ch/de/geodata/height/alti3d.html Accessed 2023-07-26

Swisstopo (2023) swissTLM3D. Federal Office of Topography swisstopo. https://www.swisstopo.admin.ch/en/geodata/landscape/tlm3d.html Accessed 2024-01-12

Swisstopo (2024) GeoMaps 500 Vector - Tectonic Map of Switzerland. Federal Office of Topography swisstopo . https://www.swisstopo.admin.ch/en/geodata/geology/maps/gk500/vector.html Accessed 2024-01-26

Swisstopo (2024) swissBOUNDARIES3D. https://www.swisstopo.admin.ch/en/landscape-model-swissboundaries3d Accessed 2024-07-10

Swisstopo (2024) WMTS-FSDI service, layer "Light base map relief". https://wmts.geo.admin.ch/EPSG/3857/1.0.0/WMTSCapabilities.xml?lang=de Accessed 2024-07-10

Swisstopo (2024) WMTS-FSDI service, layer swissALTI3D monodirectional hillshade. https://wmts.geo.admin.ch/EPSG/3857/1.0.0/WMTSCapabilities.xml?lang=de Accessed 2024-07-10

Varnes DJ (1978) Slope movement types and processes. Special Rep 176:11–33

Rossum G, Drake FL (2009) Python 3 reference manual. CreateSpace, Scotts Valley

Vakhshoori V, Zare M (2018) Is the ROC curve a reliable tool to compare the validity of landslide susceptibility maps? Geomat. Nat. Hazards Risk 9(1):249–266. https://doi.org/10.1080/19475705.2018.1424043

van Zadelhoff FB, Albaba A, Cohen D, Phillips C, Schaefli B, Dorren L, Schwarz M (2022) Introducing slideformap: a probabilistic finite slope approach for modelling shallow-landslide probability in forested situations. Nat Hazards Earth Syst Sci 22(8):2611–2635. https://doi.org/10.5194/nhess-22-2611-2022

VSS SN (1998) Swiss standard SN 670 010b. Characteristic coefficients of soils. Association of Swiss Road and Traffic Engineers, Zurich

Waser L, Ginzler C (2018). Forest Type NFI National Forest Inventory (NFI). https://doi.org/10.16904/1000001.7

Waser L, Ginzler C, Rehush N (2017) Wall-to-wall tree type mapping from countrywide airborne remote sensing surveys. Remote Sens 9(8):766. https://doi.org/10.3390/rs9080766

Wang L, Liu H (2006) An efficient method for identifying and filling surface depressions in digital elevation models for hydrologic analysis and modelling. Int J Geogr Inf Sci 20(2):193–213. https://doi.org/10.1080/13658810500433453

Watakabe T, Matsushi Y (2019) Lithological controls on hydrological processes that trigger shallow landslides: observations from granite and hornfels hillslopes in hiroshima. Japan CATENA 180:55–68. https://doi.org/10.1016/j.catena.2019.04.010

Wadoux AMJ-C, Minasny B, McBratney AB (2020) Machine learning for digital soil mapping: applications, challenges and suggested solutions. Earth-Sci Rev 210:103359. https://doi.org/10.1016/j.earscirev.2020.103359

WSL (2019) Number of natural hazard fatalities per year in Switzerland since 1946. EnviDat . https://doi.org/10.16904/envidat.33

Xiao T, Segoni S, Liang X, Yin K, Casagli N (2023) Generating soil thickness maps by means of geomorphological-empirical approach and random forest algorithm in wanzhou county. Three Gorges Reservoir Geosci Front 14(2):101514. https://doi.org/10.1016/j.gsf.2022.101514

Zappone A, Kissling E (2021) Saphyr: swiss atlas of physical properties of rocks: the continental crust in a database. Swiss J Geosci 114(1):13. https://doi.org/10.1186/s00015-021-00389-3

Zimmermann F, McArdell BW, Rickli C, Scheidl C (2020) 2d runout modelling of hillslope debris flows, based on well-documented events in switzerland. Geosci 10(2):70. https://doi.org/10.3390/geosciences10020070

Zhu A-X, Miao Y, Yang L, Bai S, Liu J, Hong H (2018) Comparison of the presence-only method and presence-absence method in landslide susceptibility mapping. CATENA 171:222–233. https://doi.org/10.1016/j.catena.2018.07.012

Zhang S, Xu Q, Zhang Q (2017) Failure characteristics of gently inclined shallow landslides in nanjiang, southwest of china. Eng Geol 217:1–11. https://doi.org/10.1016/j.enggeo.2016.11.025

## Authors and Affiliations

**Christoph Schaller[1,2] · Luuk Dorren[1] · Denis Cohen[3,4] · Arie C. Seijmonsbergen[2] · E. Emiel van Loon[2]**

✉ Christoph Schaller
christoph.schaller@bfh.ch

Luuk Dorren
luuk.dorren@bfh.ch

Denis Cohen
denis.cohen@gmail.com

Arie C. Seijmonsbergen
A.C.Seijmonsbergen@uva.nl

E. Emiel van Loon
E.E.vanLoon@uva.nl

[1] HAFL, Bern University of Applied Sciences, Länggasse 85, 3052 Zollikofen, Bern, Switzerland

[2] IBED, University of Amsterdam UVA, Sciencepark 904, 1098 XH Amsterdam, North Holland, The Netherlands

[3] CoSci LLC, Conover, WI 54519, USA

[4] Department of Earth and Environmental Science, New Mexico Tech, Socorro, NM 87801, USA